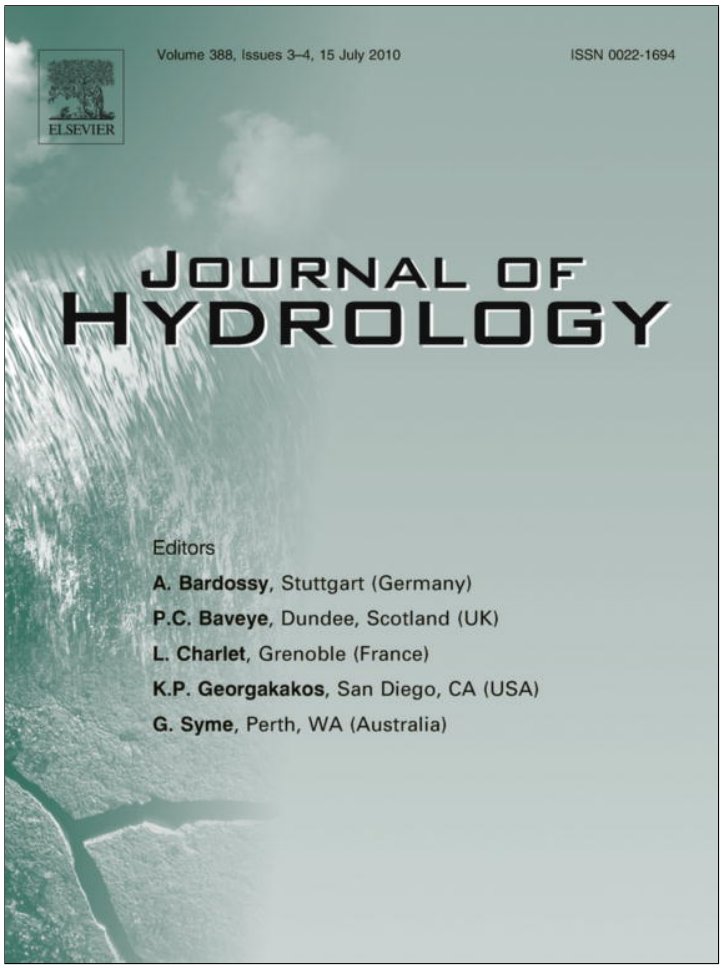

Journal of Hydrology 388 (2010) 304–320

Contents lists available at ScienceDirect

Journal of Hydrology

journal homepage: www.elsevier.com/locate/jhydrol

Equivalent hydraulic conductivity of three-dimensional heterogeneous porous media: An upscaling study based on an experimental stratigraphy

Ye Zhang [a,*], Carl W. Gable [b], Ben Sheets [c]

[a] Department of Geology and Geophysics, University of Wyoming, Laramie, WY 82071, USA
[b] EES-6, MS T003, Los Alamos National Lab, Los Alamos, NM 87545, USA
[c] School of Oceanography, University of Washington, Seattle, WA 98195, USA

ARTICLE INFO

Article history:
Received 1 June 2009
Received in revised form 16 February 2010
Accepted 5 May 2010

This manuscript was handled by P. Baveye, Editor-in-Chief, with the assistance of D.P. Ahlfeld, Associate Editor

Keywords:
Hydraulic conductivity
Heterogeneity
Experimental stratigraphy
Equivalent conductivity
Effective conductivity
Connectivity

SUMMARY

A critical issue facing large scale numerical simulation models is the estimation of representative hydraulic conductivity to account for the unresolved sub-grid-scale heterogeneity. In this study, two experiment-based hydraulic conductivity models offer a test case to evaluate this parameter. Each model contains a different heterogeneity pattern with connectivity characteristics that cannot be captured by univariate and bivariate statistics. A three-dimensional numerical upscaling method was developed to compute an equivalent conductivity full tensor for each model. The equivalent conductivities were compared to direct averages of local conductivities and to an effective conductivity predicted by several analytical methods. For each model, $\ln K$ variances up to 16 were evaluated. The impact of variance on both upscaled conductivity and three fluid flow connectivity factors was assessed. Results suggest: (1) the upscaling method gave reliable results comparable to an established method which only gives the diagonal components, (2) for both aquifer models, when $\ln K$ variances are low (less than 1.0), all analytical methods evaluated are nearly equally accurate; however, when variance becomes higher, the analytical methods of Desbarats (1992) and Noetinger and Haas (1996) were found to provide robust estimates of equivalent conductivities, despite possible violation of the multiGaussian assumption, (3) fluid flow characteristics in each model were significantly impacted by increasing variance, which can result in flow channeling in the lateral direction and increasing global anisotropy ratios of the equivalent conductivity, and (4) geometric connectivity, as analyzed by a percolation cluster analysis, indicates the importance of such features in focusing flow, in addition to the effects of high variance.

1. Introduction

Regional groundwater flow models require the assignment of hydraulic conductivities to large simulation grid cells used to discretize the flow domain. However, conductivity of the porous media is often measured at smaller scales via, e.g., permeameter, flowmeter, or borehole geophysical tests. Based on such measurements, the method of finding representative conductivities for the large simulation grid cells is called upscaling. A similar development in petroleum engineering is to upscale the intrinsic permeability for the coarse grids of a multiphase flow simulator (e.g., Christie, 1996; Pickup and Hern, 2002; Durlofsky, 2005; Gerritsen and Durlofsky, 2005; Chen and Durlofsky, 2006; Wen et al., 2006). Due to the nonlinear nature of the coupled flow equations and the multiple degrees of freedom solved, reservoir simulation imposes more stringent constraint on the grid size. For reservoirs where subsurface property data are available, a common practice is to develop a fully heterogeneous fine-grid geocellular model using geostatistical techniques. This model is then upscaled to a coarse grid for flow simulations. Regardless of the goal, i.e., groundwater studies or petroleum reservoir modeling, an important step is to find large-scale equivalent conductivity (or permeability) based on small-scale measurements or stochastically generated images at the subgrid level.

Numerous methods have been developed to estimate equivalent hydraulic conductivity for heterogenous porous media (*see reviews,* Wen and Gómez-Hernández, 1996; Renard and de Marsily, 1997; Sanchez-Vila et al., 2006). The equivalent conductivity differs from an effective conductivity which is defined within a stochastic context where the small-scale conductivity heterogeneity is treated as a random space function (RSF) (e.g., Dagan, 1989; Gelhar, 1993; Zhang, 2002). The effective conductivity can be estimated from the spatial correlation and variability characteristics of the RSF. It is considered an intrinsic property of the RSF, thus

* Corresponding author. Tel.: +1 307 766 2981; fax: +1 307 766 2697.
E-mail address: yzhang9@uwyo.edu (Y. Zhang).

0022-1694/$ - see front matter © 2010 Elsevier B.V. All rights reserved.
doi:10.1016/j.jhydrol.2010.05.009

independent of the boundary condition and domain size. On the other hand, the equivalent conductivity represents a fictitious homogenous medium that preserves the mean flux of the heterogenous deposit under a given head gradient. Compared to effective conductivity, the estimation of the equivalent conductivity does not require restrictive assumptions on the RSF or the flow condition (e.g., stationarity, mean uniform flow). This is useful for upscaling deposits that exhibit complex spatial heterogeneities and long range correlations, i.e., when problem size is finite compared to the conductivity correlation ranges. However, equivalent conductivity depends on the boundary condition, thus it is not unique. It may approach the effective conductivity when the domain size is large compared to the conductivity correlation range (Renard and de Marsily, 1997).

In this study, based on an experimental stratigraphy, two three-dimensional (3D) synthetic aquifer models were evaluated for both equivalent conductivity and fluid flow connectivity. Both models are statistically anisotropic while each contains a different heterogeneity pattern. One, in particular, contains a high-conductivity connected structure that cannot be captured by univariate and bivariate statistics. A 3D numerical upscaling method was used to compute a full-tensor equivalent conductivity for each model. The method extends an earlier approach developed for upscaling two-dimensional datasets (Zhang et al., 2006, 2007). The computed equivalent conductivities were compared to direct averages of local conductivities, and to an effective conductivity predicted by several analytical methods applicable to upscaling three-dimensional statistically *anisotropic* media. As reviewed by prior authors, though a vast literature exists for estimating equivalent or effective conductivity, few analytical methods are applicable to upscaling statistically anisotropic media. For such media, due to anisotropy, the equivalent or effective conductivity are usually tensor quantities, thus methods developed for isotropic media do not apply. Since for many problems encountered in field and large scale simulation studies, anisotropic systems are common (Durlofsky, 1991, 2005; Pickup et al., 1994; Pickup and Hern, 2002; Kerrou et al., 2008), significant practical interest exists in understanding the upscaling of such systems that also contain geologically realistic heterogeneity. The analytical methods investigated in this study were either developed or proposed for such media. Compared to numerical upscaling, the main advantage of the analytical methods is their ability to predict large-scale conductivity without detailed simulations.

In this study, a sensitivity analysis was conducted for each aquifer model by increasing the natural log conductivity ($\ln K$) variance to represent systems ranging from weakly heterogeneous to strongly heterogeneous (Gelhar, 1993). Given the same heterogeneity pattern, high $\ln K$ variance should exert significant influence on the simulated flow fields. Herein, such effects were evaluated systematically for the two synthetic aquifers. Thus an important contribution of this work is to provide constraints on the applicability of the (anisotropic) analytical methods under increasing heterogeneity variance and for different heterogeneity patterns. Further, since one of the aquifer models exhibits a significant large-scale connectivity, the effects of geometric connectivity along with high $\ln K$ variance on several fluid flow connectivity factors were assessed. We explore the conditions under which preferential flow pathways will form in the simulated flow fields.

Using synthetic aquifer models to reveal insights on subsurface flow, transport, and parameter scaling is a well-known approach in understanding naturally inaccessible and heterogeneous systems (e.g., Scheibe and Freyberg, 1995; Christie and Blunt, 2001). In sandstones, correlation was found to exist between sedimentary structures and permeability (Hurst and Rosvoll, 1991; Moreton et al., 2002). In particular, high-resolution photomosaics can correspond to detailed natural log permeability measurements (Coskun and Wardlaw, 1992; Makse et al., 1996; Tidwell and Wilson, 1997). Synthetic models have been created based on images of sediment outcrops and used in upscaling studies (Pickup and Hern, 2002) or geostatistical reservoir analysis (Deutsch, 2002). What is unique about our series of studies is that our conductivity models correspond to physical stratigraphies created by sediment transport experiments in a laboratory flume. In the current study, a new stratigraphic dataset was analyzed (our previous works had analyzed a prototype deposit created in an earlier experiment). In all experiments, however, deposits were formed by sedimentary processes that represent subsets of those active in nature. These include important forms of self-organization and spontaneous pattern formation that are common in nature yet difficult to capture using stochastic simulations. The experimental stratigraphies thus exhibit multiscale variability that may not satisfy many statistical assumptions used by stochastic algorithms to generate synthetic deposits (e.g., stationarity, multiGaussian distributions) (e.g., Deutsch and Journel, 1997). The two aquifer models of this study, developed based on the experimental stratigraphies, will enable us to understand how diversity in sedimentary heterogeneity, when translated to hydraulic conductivity and scaled for variability, may result in different fluid flow and upscaling behavior.

In the reminder of the text, the sediment experiment that created the experimental deposit was described first, followed by the procedure used to create the two synthetic aquifer models. The 3D numerical upscaling method was introduced, along with a description of the analytical methods evaluated. Three connectivity flow factors were defined, followed by the Results section where flow simulation outcomes, upscaled conductivities (both numerical and analytical predictions), and flow connectivity factors were presented. Directions for future research were described in the end.

2. Methods

2.1. Sediment experiment

The experimental stratigraphy used for this study was produced in a sediment experiment conducted in 1999 at the Saint Anthony Falls Hydraulics Laboratory, University of Minnesota. The experiment was designed to isolate the influence of various extrinsic controls on stacking patterns in alluvial stratigraphy (e.g., Paola, 2000; Cazanacli et al., 2002; Sheets et al., 2002; Hickson et al., 2005; Strong et al., 2005) (Fig. 1; top panel). Two sediment types were used, a quartz sand and anthracite coal, which generally simulated coarse-grained and fine-grained bedload sediments, respectively. While the experiment was not designed as a direct scale model of any particular natural system, the processes are broadly analogous to those observed in modern alluvial systems. That is, general fluvial morphological characteristics such as longitudinal grain size fining, channelized flows, and overbank flows were well developed in the experiment. As such, we consider the experimental stratigraphy a good testing ground for the upscaling techniques presented herein.

After the deposits were formed, they were dissected every 2 cm in the direction perpendicular to sediment transport and imaged with high resolution to create a digital representation of the stratigraphy (Fig. 1; bottom panel). While this process and the stratigraphy have been described in more details elsewhere (Sheets et al., 2002; Hickson et al., 2005), we would note here that the deposits of the experimental system are dominated by the low aspect ratio (width:depth) channel bodies and high aspect ratio depositional sheets. The two modes correlate to scour and deposition associated with channelized and unchannelized (overbank) flows, respectively (Sheets et al., 2007).

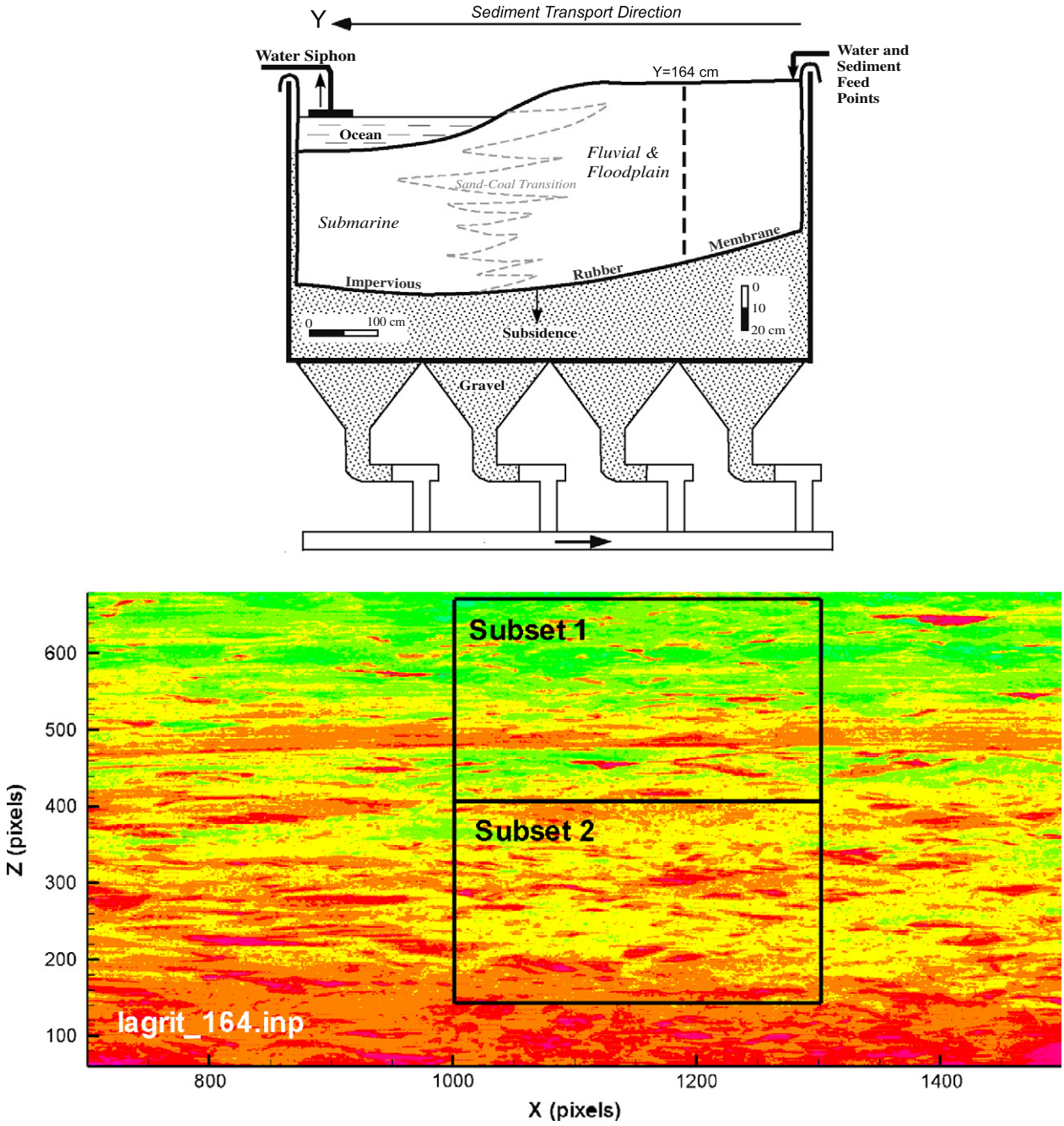

Fig. 1. Schematic diagram of the experimental apparatus used in the sediment transport experiment (top). Vertical line indicates the position of an image scan of the stratigraphy at 164 cm downstream from the sediment sources (bottom). Green, yellow and red correspond to increasing brightness of the image, thus increasing sand content of the stratigraphy. Two boxes indicate the locations of the two subsets used in this study. To create the third dimension, 15 additional transects parallel to this stratigraphy were used, each separated by 2 cm.

In this study, two 3D models of hydraulic conductivity heterogeneity were created, based on two subsets of the digital stratigraphy (Fig. 1). The subsets were selected from the upstream fluvial portion of the deposits which exhibited significant sedimentary structures (e.g., channel, floodplain, sheetflow deposits). The downstream marine deposition tended to be dominated by clay settling, thus containing less heterogeneities. This choice of model sites was considered reasonable since this study focuses on the effects of heterogeneity and connectivity. Further, subset 1 was selected from the upper channel–floodplain belt, directly above subset 2 (Fig. 1; bottom). It lies within a region of the stratigraphy that is dominated by sheetflow and floodplain deposits. Along the transect shown (Fig. 1), a significant lateral sand-rich structure exists in the lower region of this subset, spanning across the *X* direction. On the other hand, subset 2 lies within the lower channel belt, deposited in a region that is more sand-rich and contains numerous channels. These channels are generally small, with widths (in the *X* direction) ranging from 30 to 100 pixels. Subset 2 is of the same dimensions as subset 1.

To create the third dimension for each subset, 16 image transects perpendicular to sediment transport (thus parallel to the stratigraphy of Fig. 1) were stacked. To allow smooth transitions, linear interpolations between the 16 transects were conducted. Note that the dissection of the stratigraphy and subsequent

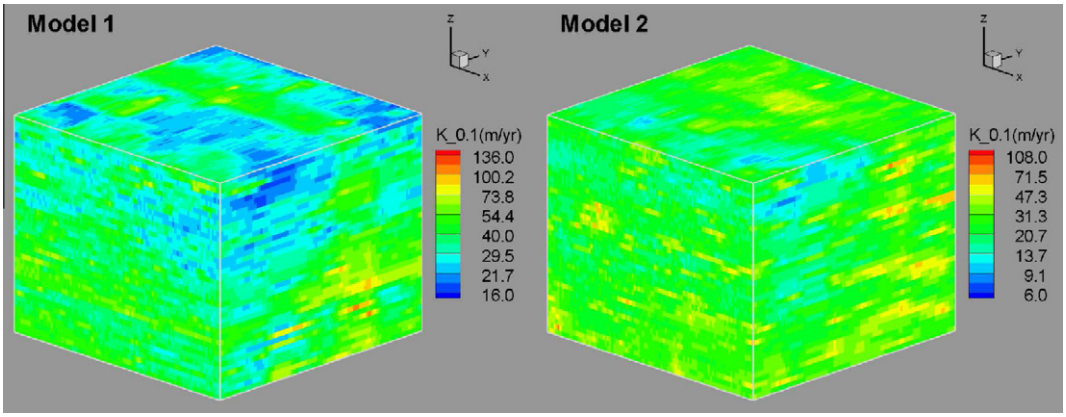

Fig. 2. Visualization of the two models, both scaled to a ln$K$ variance of 0.1.

imaging were carefully coordinated within a single global coordinate, thus the transects were able to be stacked precisely. Their positions along the Y axis (Fig. 1) were: Y = 146, 148, 150, 152, 154, 156, 158, 160, 162, 164, 168, 170, 172, 174, 176, 178, 180 cm, with increasing distance from the upstream sediment feeders. Y = 166 cm was not included since during the dissection of the stratigraphy, a portion of the deposit collapsed and thus could not be imaged. Conceivably, the stratigraphic information interpolated between 164 and 168 could contain some minor artifacts and alignment issues, though we have not been able to visually detect them.

2.2. Model construction

In this study, each subset was coarsened to a simulation model grid using the gridding toolbox *lagrit* (www.lagrit.lanl.gov), for two reasons: (1) the stratigraphy was scanned in high resolution, thus each image pixel has a grayscale corresponding to the average light reflection of a few dozen sand grains, which is beneath the continuum scale for flow modeling; and (2) each subset contained 2.88 million image pixels, considered large for the 3D full-tensor upscaling procedure of this study which involves many flow experiments. Using the lagrit "Interpolate" function, the grayscale of the grid cell of the coarse simulation model was computed based on linear interpolation of those of the enclosed fine-grid pixel cells. After the interpolation, two models of equal dimensions were created: Model 1 coarsened from subset 1, Model 2 coarsened from subset 2 (Fig. 2). Each model has 101 by 101 by 41 grid cells in the x, y, and z directions, respectively. Each thus has a total of 418,241 grid cells, efficient for upscaling calculations. After coarsening, though the shapes of many small-scale structures (e.g., the tiny channels in subset 2) became less distinct, significant large-scale connectivity was preserved (Fig. 2).

Following the approach adopted in our previous studies (Zhang et al., 2005b, 2006, 2007; Zhang and Gable, 2008; Zhang, 2008), the grid cells of each simulation model assume fixed length scales to represent a local representative elementary volume (REV) upon which a local, scalar hydraulic conductivity can be defined. Depending on the domain size of interest (e.g., field scale up to basin scale), the grid cell can assume sizes ranging from a few cm to hundreds of m. In this study, the simulation model cells were assigned: $\Delta x = \Delta y = 25.0$ m and $\Delta z = 2.5$ m, thus the model domain dimensions are $2500 \times 2500 \times 100$ m^3. These dimensions lie within the range of grid cell sizes for regional- to basin-scale flow simulators (e.g., Zhang et al., 2005a, 2006). And, using the grid-cell grayscale and two appropriately chosen end member conductivities (one for pure sand, with the highest grayscale; one for pure clay, with the lowest grayscale), a scalar local conductivity was obtained for each cell via log-linear interpolation (detailed discussions on this and alternative interpolation methods can be found

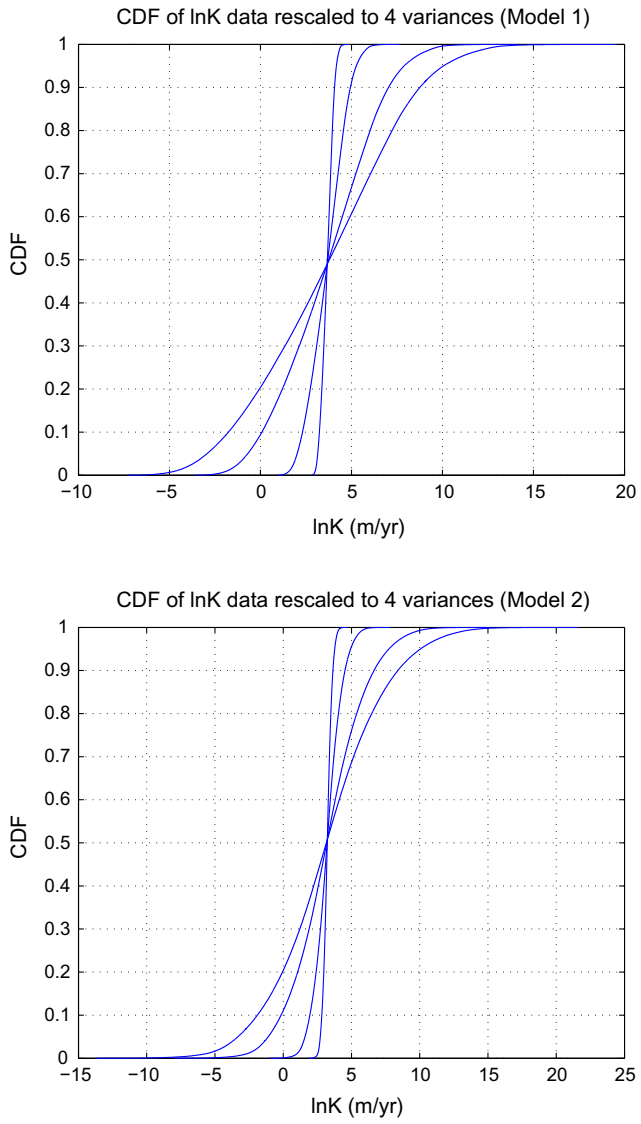

Fig. 3. Cumulative distribution function of ln$K$ for four increasing variances (Var[ln$K$] = 0.1, 1.0, 7.0, 16.0), for Models 1 and 2.

in Zhang et al. (2005b)). A synthetic hydraulic conductivity model was thus created from each subset. Each model exhibits a different spatial pattern and connectivity in hydraulic conductivity (Fig. 2), its end member conductivities varied as part of a sensitivity analysis to create different variability levels in the model.

Besides the concerns of capturing heterogeneity and connectivity (where models were selected from different regions of the experimental stratigraphy based on visual inspection), two additional criteria were used to create the models: (1) The model domain in all three dimensions was relatively large compared to the respective $\ln K$ integral scales ($\lambda_x, \lambda_y, \lambda_z$). The integral scales were estimated by conducting a geostatistical analysis on the $\ln K$ field (next). In both models, ratio of the domain length scale to the integral scale is much larger than 4.0, minimizing the possible impact of specified boundary conditions on numerical upscaling results. This criterion was used in upscaling studies for both statistically isotropic (Rubin and Dagan, 1988) and anisotropic media (Paleologos et al., 1996; Sarris and Paleologos, 2004). It ensures that numerical upscaling results of bounded domains can be compared to analytic-stochastic theory predictions for unbounded problems (Zhang et al., 2006). (2) For each model, though coarsened from the subset, its grid discretization was still resolved enough such that the lateral $\ln K$ integral scale was represented by greater than $5 \sim 10$ grid cells in each direction (Desbarats, 1992).

In this study, both conductivity models were analyzed for upscaling and flow connectivity characteristics. The connectivity characteristics were then compared between models to determine a quantitative metric that can be used to verify the observed differences in connectivity, i.e., the channel–sheetflow–floodplain pattern versus the more channelized pattern. For each model, $\ln K$ histogram was unimodal and can be approximated well by a Gaussian probability density function (not shown). The variability of each model was scaled to four global $\ln K$ variances (0.1, 1.0, 7.0, 16.0), while keeping the same global mean $\ln K$ value (Fig. 3). By varying the variance while maintaining the same heterogeneity pattern, each model reflects a full range of systems from weakly heterogeneous to strongly heterogeneous. The scaling of variance should exert a significant impact on flow, as higher variance increases the contrast of conductivity between the interbedded sand-rich and clay-rich facies, thus potentially focusing flow through connected high-K zones in the model. The low variance systems, on the other hand, should behave more like a homogeneous deposit, despite the existence of the same geometric connectivity which is not affected by variance scaling.

2.3. Spatial correlations

Geostatistical characteristics of the models were evaluated by computing three directional experimental $\ln K$ variograms for each model: two horizontal; one vertical (Figs. 4 and 5). In these figures, $\ln K$ variance for each model is 0.1. Note that scaling the variance will proportionally scale the variogram sill without affecting the correlation ranges. For each model, the directional integral scales were thus obtained from fitting an exponential function to each directional experimental variogram. For Model 1, $\lambda_x = 155.0$ m, $\lambda_y = 690.0$ m, and $\lambda_z = 5.0$ m. For Model 2, $\lambda_x = 155.0$ m, $\lambda_y = 450.0$ m, and $\lambda_z = 3.5$ m. Both the integral scales and the associated statistical anisotropy ratios (e.g., λ_x/λ_z, λ_y/λ_z) fall within the range found for natural braided fluvial deposits (Deutsch, 2002), suggesting that the grid cell size and aspect ratio chosen in this study are reasonable. In this study, these correlation parameters will be used by several analytical methods to predict an effective conductivity, to be compared to the results of numerical upscaling.

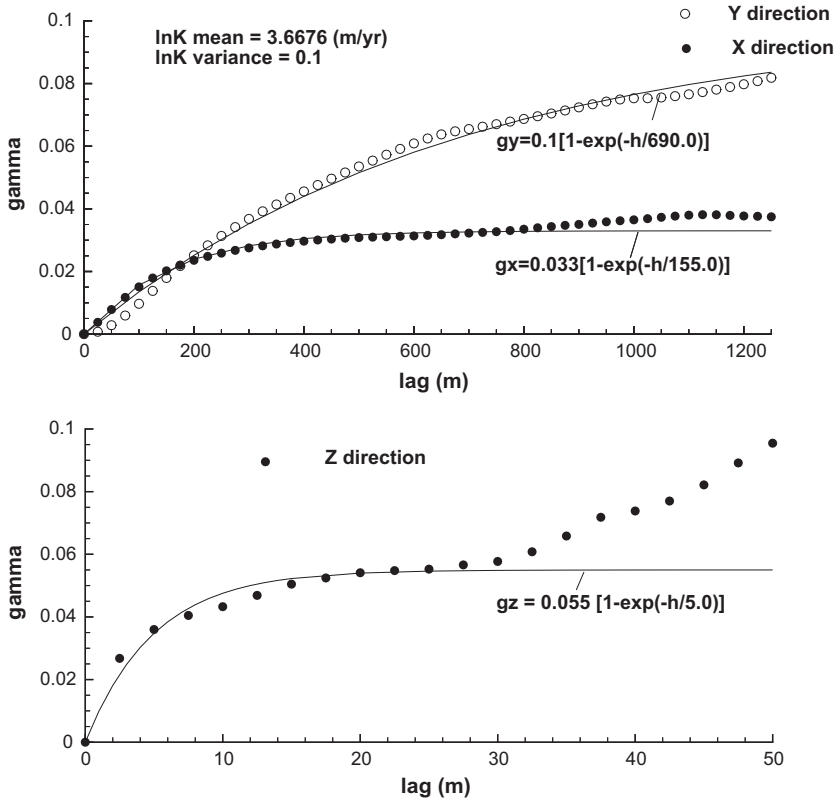

Fig. 4. Directional experimental variograms of $\ln K$ for Model 1, shown as circles. Three exponential variogram models are fitted (curves), with the fitted functions shown. For the variogram calculations, variance of $\ln K$ in the aquifer is 0.1.

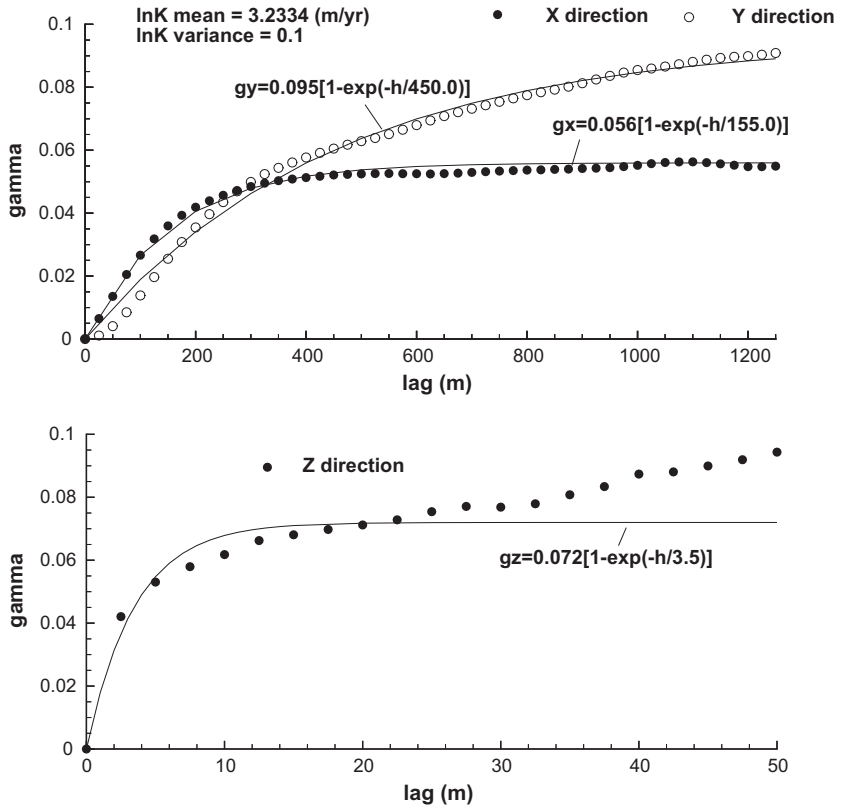

Fig. 5. Directional experimental variograms of ln*K* for Model 2, shown as circles. Three exponential variogram models are fitted (curves), with the fitted functions shown. For the variogram calculations, variance of ln*K* in the aquifer is 0.1.

For each model, both horizontal integral scales are significantly larger than the vertical integral scale, attesting to the observed sedimentary stratification. In both models, a distinct zonal anisotropy exists in the horizontal direction, i.e., sills of the *x*-direction experimental variogram are lower than those of the *y*-direction variogram. This indicates potential long-range correlation along *x* beyond the size of the model domain, which is not represented by the fitted variogram functions. Instead, a stationary model was fitted to capture variogram values at shorter lags near the origin where more data pairs were available. This is important for the accurate determination of correlation ranges within each aquifer model (or, the sub-grid-level heterogeneity scales as would be estimated for the grid blocks of a large field simulator). Moreover, in Model 1, the spatial correlation structure is not axisymmetric, i.e., the horizontal integral scales are not equal. The same is observed for Model 2. Comparing the correlation structures between models, their overall correlation characteristics are similar, e.g., the approximately exponential rise of the variograms towards the sills (Figs. 4 and 5). Clearly, as previous studies have demonstrated (e.g., Gomez-Hernandez and Wen, 1998; Knudby and Carrera, 2005, 2006), two-point correlation functions cannot distinguish either the existence or lack of existence of important spatial connectivity as observed in the models (Fig. 2). In this study, besides visual inspection, such geometric connectivity will be quantified by a connectivity flow factor via a percolation cluster analysis.

2.4. Numerical upscaling

Upscaling for 3D full-tensor hydraulic conductivity was conducted using numerical flow experiments, in extension to an earlier method developed to upscale two-dimensional datasets (Zhang et al., 2006). To find the equivalent conductivity ($\mathbf{K}^*$) for each model, a series of single-phase, steady-state, and incompressible flow simulations was conducted by varying the boundary conditions along the periphery of the heterogeneous aquifer model. An equivalent conductivity was obtained by incorporating results from all simulations. Specifically, under a fixed boundary condition, a set of equations was assembled based on the global Darcy's Law (assumed to be applicable at both scales), each consisting of spatially averaged directional hydraulic gradients, Darcy fluxes, and equivalent conductivity tensor components:

$$
\begin{aligned}
B.C.1: &\begin{Bmatrix} \langle q_x\rangle_1 \\ \langle q_y\rangle_1 \\ \langle q_z\rangle_1 \end{Bmatrix} = -\begin{bmatrix} K_{xx} & K_{xy} & K_{xz} \\ K_{yx} & K_{yy} & K_{yz} \\ K_{zx} & K_{zy} & K_{zz} \end{bmatrix} \begin{Bmatrix} \langle \partial h/\partial x\rangle_1 \\ \langle \partial h/\partial y\rangle_1 \\ \langle \partial h/\partial z\rangle_1 \end{Bmatrix} \\
B.C.2: &\begin{Bmatrix} \langle q_x\rangle_2 \\ \langle q_y\rangle_2 \\ \langle q_z\rangle_2 \end{Bmatrix} = -\begin{bmatrix} K_{xx} & K_{xy} & K_{xz} \\ K_{yx} & K_{yy} & K_{yz} \\ K_{zx} & K_{zy} & K_{zz} \end{bmatrix} \begin{Bmatrix} \langle \partial h/\partial x\rangle_2 \\ \langle \partial h/\partial y\rangle_2 \\ \langle \partial h/\partial z\rangle_2 \end{Bmatrix} \\
&\cdots \qquad\qquad\qquad \cdots \\
B.C.m: &\begin{Bmatrix} \langle q_x\rangle_m \\ \langle q_y\rangle_m \\ \langle q_z\rangle_m \end{Bmatrix} = -\begin{bmatrix} K_{xx} & K_{xy} & K_{xz} \\ K_{yx} & K_{yy} & K_{yz} \\ K_{zx} & K_{zy} & K_{zz} \end{bmatrix} \begin{Bmatrix} \langle \partial h/\partial x\rangle_m \\ \langle \partial h/\partial y\rangle_m \\ \langle \partial h/\partial z\rangle_m \end{Bmatrix}
\end{aligned}
\tag{1}
$$

where $\langle\rangle$ represents spatial averaging; q_x, q_y, q_z are components of the Darcy flux; h is hydraulic head; subscripts $_{1,2,\ldots,m}$ denote a particular flow experiment; $K_{xx},\ldots,K_{zz}$ are components of the upscaled equivalent conductivity $\mathbf{K}^*$. Following Zhang et al. (2006), the above equations is rewritten as:

$$\begin{bmatrix} \langle \partial h/\partial x\rangle_1 & \langle \partial h/\partial y\rangle_1 & \langle \partial h/\partial z\rangle_1 & 0 & 0 & 0 & 0 & 0 & 0 \\ 0 & 0 & 0 & \langle \partial h/\partial x\rangle_1 & \langle \partial h/\partial y\rangle_1 & \langle \partial h/\partial z\rangle_1 & 0 & 0 & 0 \\ 0 & 0 & 0 & 0 & 0 & 0 & \langle \partial h/\partial x\rangle_1 & \langle \partial h/\partial y\rangle_1 & \langle \partial h/\partial z\rangle_1 \\ \langle \partial h/\partial x\rangle_2 & \langle \partial h/\partial y\rangle_2 & \langle \partial h/\partial z\rangle_2 & 0 & 0 & 0 & 0 & 0 & 0 \\ 0 & 0 & 0 & \langle \partial h/\partial x\rangle_2 & \langle \partial h/\partial y\rangle_2 & \langle \partial h/\partial z\rangle_2 & 0 & 0 & 0 \\ 0 & 0 & 0 & 0 & 0 & 0 & \langle \partial h/\partial x\rangle_2 & \langle \partial h/\partial y\rangle_2 & \langle \partial h/\partial z\rangle_2 \\ \cdots & \cdots & \cdots & \cdots & \cdots & \cdots & \cdots & \cdots & \cdots \\ \langle \partial h/\partial x\rangle_m & \langle \partial h/\partial y\rangle_m & \langle \partial h/\partial z\rangle_m & 0 & 0 & 0 & 0 & 0 & 0 \\ 0 & 0 & 0 & \langle \partial h/\partial x\rangle_m & \langle \partial h/\partial y\rangle_m & \langle \partial h/\partial z\rangle_m & 0 & 0 & 0 \\ 0 & 0 & 0 & 0 & 0 & 0 & \langle \partial h/\partial x\rangle_m & \langle \partial h/\partial y\rangle_m & \langle \partial h/\partial z\rangle_m \end{bmatrix} \cdot \begin{Bmatrix} K_{xx} \\ K_{xy} \\ K_{xz} \\ K_{yx} \\ K_{yy} \\ K_{yz} \\ K_{zx} \\ K_{zy} \\ K_{zz} \end{Bmatrix} = - \begin{Bmatrix} \langle q_x\rangle_1 \\ \langle q_y\rangle_1 \\ \langle q_z\rangle_1 \\ \langle q_x\rangle_2 \\ \langle q_y\rangle_2 \\ \langle q_z\rangle_2 \\ \cdots \\ \langle q_x\rangle_m \\ \langle q_y\rangle_m \\ \langle q_z\rangle_m \end{Bmatrix} \quad (2)$$

The nine equivalent conductivity components were thus obtained by solving the above equation. Note that to obtain unique solutions, the total number of flow experiments m must be $\geqslant 3$: when $m = 3$, Eq. (2) was solved exactly; when $m > 3$, Eq. (2) was solved via least square solution. As in the previous studies (Zhang et al., 2006, 2007), symmetry was imposed, i.e., an average of the symmetrical off-diagonal terms (e.g., K_{xy} and K_{yx}) was taken and assigned to its respective position in the upscaled conductivity. This is not an unreasonable approach. Due to the lateral stratification exhibited by both aquifer models, the equivalent conductivity was diagonally dominant (see Section 3). Thus, for each model, under a fixed global $\ln K$ variance, a symmetric full tensor was evaluated in this study.

Since numerical upscaling results will be compared to analytical expressions developed for uniform flow conditions (those developed for radial flows were not investigated in this study), linear flood patterns were appropriate in the flow experiments. In the simulations conducted for each model, to assemble Eq. (2), three sets of global boundary conditions were used ($m = 3$): (1) x-flow (specified heads along the left and right faces of the model; no-flow on all other faces); (2) y-flow (specified heads along the front and back faces; no-flow on all other faces); and (3) z-flow (specified heads along the top and bottom faces; no-flow on all other faces). The specified heads were selected such that in each flow experiment (whether it is x-flow, y-flow, or z-flow), flow was driven towards the positive axis. In each experiment, a fixed head of 100.0 and 10.0 m was assigned to the inflow and outflow boundaries, respectively.

A 3D Finite Difference flow simulator was developed with a seven-point block-centered scheme (Desbarats, 1992; Sarris and Paleologos, 2004). It was first verified by solving equivalent conductivities for problems with known analytical solutions. In one problem, each local K was homogeneous, thus the equivalent conductivity computed remained the same as the local conductivity. In a second problem, local K was deterministically generated to create a perfectly layered deposit with units of equal thickness. In this case, the equivalent lateral conductivities were verified to be the arithmetic mean of the local layer K, and the equivalent vertical conductivity verified to be the harmonic mean of the local layer K. In this study, to further verify the upscaling results of the two aquifer models, equivalent $\mathbf{K}^*$ was also computed using the well-established Simple Laplacian method which can determine a diagonal tensor for a block medium (Wen and Gómez-Hernández, 1996). Since the heterogeneities in our models were dominated by horizontal stratification, the Simple Laplacian method should provide values close to the diagonal components of the full tensor $\mathbf{K}^*$ computed with Eq. (2).

2.5. Analytical upscaling

Numerical upscaling results of the equivalent conductivity were first compared to two sets of analytical bounds (Renard and de Marsily, 1997): (1) The Wiener bounds: $[K_H, K_A]$, where K_H and K_A are the harmonic and arithmetic means of the local conductivities, respectively. The Wiener bounds are valid for predicting the equivalent conductivity components for the end-member cases of flow parallel (K_A) and perpendicular (K_H) to perfect layers of uniform thickness. (2) Cardwell and Parsons bounds: $\mu_H^x(\mu_A^z(\mu_A^y)) \leqslant K_{jj} \leqslant \mu_A^z(\mu_A^y(\mu_H^x))$. The lower bound is calculated by the harmonic mean of the arithmetic means of the point K, along the given directions indicated (first y, then z, then x); the upper bound is calculated similarly. This bounds is suitable for determining the equivalent conductivity range for a block domain. Other analytical bounds also exist (Renard and de Marsily, 1997), though most are restricted to statistically isotropic media, binary media, or media of lower spatial dimensions. The more general bounds were thus chosen to compare with the numerical results. As upscaling of both models will demonstrate, most equivalent conductivities are diagonally dominant. Therefore, only the principal components of $\mathbf{K}^*$ (subsequently labeled as K_{11}, K_{22}, and K_{33}) were compared to the bounds. This also applies to the comparison with the predictions of select analytical methods (next).

Besides simple bounds, several analytical methods exist that are applicable to upscaling three-dimensional statistically anisotropic media. In the following paragraphs, these methods were introduced by grouping them based on similarity in approaches. Within a stochastic framework, the local point-scale conductivities $K(\mathbf{x})$ can be defined as a RSF. A natural log transform is then used: $f = Y(\mathbf{x}) = \ln K(\mathbf{x})$, also a RSF. If $Y(\mathbf{x})$ is assumed to be stationary, ergodic, and multivariate Gaussian, its first and second spatial moments are:

$$E[Y(\mathbf{x})] = \mu_f \quad (3)$$

$$Cov[Y(\mathbf{x}), Y(\mathbf{x}+\mathbf{h})] = \sigma(\mathbf{h}) \quad (4)$$

$$Var[Y(\mathbf{x})] = \sigma(\mathbf{0}) = \sigma_f^2 \quad (5)$$

$$\gamma(\mathbf{h}) = \sigma_f^2 - \sigma(\mathbf{h}) \quad (6)$$

where μ_f and σ_f^2 are the expected value and variance of the point-scale $\ln K$, respectively. $\sigma(\mathbf{h})$ and $\gamma(\mathbf{h})$ are the spatial covariance function of $\ln K$ and its variogram, respectively. Under these conditions, an ensemble power mean of $K(\mathbf{x})$ can be obtained: $K_\omega = E[K(\mathbf{x})^\omega]^{1/\omega}$, where ω is the power-averaging exponent. An effective block-scale conductivity K_V can further be defined over volume V. After defining

an ensemble variogram $\bar{\gamma} = (1/V^2)\int_V \int_V \gamma(|r-s|)dr\,ds$, an expected value of K_V is obtained (Desbarats, 1992):

$$E[K_V] \simeq K_\omega \exp\left[\frac{1-\omega}{2}\left(\sigma_f^2 - \bar{\gamma}\right)\right] \tag{7}$$

When V is infinite, the ensemble variogram approaches the variance, and $E[K_V] \simeq K_\omega$. Thus, for a large block, K_V can be written as a spatial power average of the local point-scale conductivities $K(\mathbf{x})$:

$$K_V = \left(\frac{1}{V}\int_V K(\mathbf{x})^\omega dV\right)^{1/\omega} \quad \omega \neq 0 \tag{8}$$

$$K_V = \exp\left(\frac{1}{V}\int_V \ln K(\mathbf{x})dV\right) \quad \omega = 0 \tag{9}$$

The above second equation is the limit of the first equation when $\omega \to 0$. Note that K_ω is the asymptotic limit of Eq. (8) (Desbarats, 1992). In this study, to compute the block conductivity principal components for the two aquifer models which are discretized in space, the above equations can be written in the discrete form and further generalized to account for tensor components:

$$K_{jj} = \left[\frac{1}{N}\sum_{i=1}^{N} K_i^{\omega_j}\right]^{1/\omega_j} \quad (j = 1,\ldots,3)\ \ \omega_j \neq 0 \tag{10}$$

$$K_{jj} = K_G = \exp\left[\frac{1}{N}\sum_{i=1}^{N} \ln K_i\right] \quad (j = 1,\ldots,3)\ \ \omega_j = 0 \tag{11}$$

where N is the number of local conductivities (K_i), K_{jj} represent the principal components of the block conductivity, ω_j represent the corresponding directional power-averaging exponents. Note that $-1 \leqslant \omega_j \leqslant 1$: when $\omega_j = -1$, $K_{jj} = K_H$; $\omega_j = 1$, $K_{jj} = K_A$; when $\omega_j \to 0$ in the limit, K_{jj} is the geometric mean (K_G). Further, in multiGaussian media with low variance, an approximate relation of Eq. (10) was found (Desbarats, 1992):

$$\ln(K_{jj}) \simeq \mu_f + \frac{\omega_j}{2}\sigma_f^2 \quad (j = 1,\ldots,3) \tag{12}$$

The validity of this equation can be tested by applying the directional exponent of Eqs. (10) and (12), i.e., equating K_{jj} with numerical obtained values and finding the corresponding ω_j for Eq. (12). Despite being an approximate equation, it predicted accurate results for both isotropic and anisotropic correlation structures, and for σ_f^2 up to 4.0 (Desbarats, 1992). Based on the Green's function formulation, a similar expression was developed for a multiGaussian medium of large extent (e.g., domain length greater than $\ln K$ integral scales) (Noetinger and Haas, 1996):

$$K_{jj} \simeq K_G \exp\left(\omega_j \sigma_f^2/2\right) \quad (j = 1,\ldots,3) \tag{13}$$

Eq. (13) was numerically verified by the above authors to be accurate for media with variances up to 1.0. Finally, within a similar power-averaging framework, Ababou (1991) had earlier on proposed a formulation for estimating ω_j:

$$\omega_j = 1 - \frac{2}{3}\frac{\lambda_{Harmo}}{\lambda_j} \quad (j = 1,\ldots,3) \tag{14}$$

where λ_j represent the directional $\ln K$ integral scales, λ_{Harmo} is their harmonic mean estimated by $\lambda_{Harmo} = \left[\frac{1}{3}\sum_{j=1}^{3}\lambda_j^{-1}\right]^{-1}$. Eqs. (10)–(14) can be used to predict block conductivity principal components, given local conductivities and directional $\ln K$ correlation ranges. In this study, these parameters can be readily estimated for the aquifer models.

Besides the above power-averaging based approaches, analytical-stochastic expressions were also developed using perturbation analyses to relate the effective conductivity to K_G, σ_f^2, and $\ln K$ integral scales. For a stationary medium with low variance, a well-known result is (Gelhar, 1993):

$$K_{jj} = K_G\left[1 + \sigma_f^2\left(\frac{1}{2} - g_{jj}\right)\right] \quad (j = 1,\ldots,3) \tag{15}$$

where g_{jj} is a complex multidimensional integral. For an axisymmetrical medium (e.g., $\lambda_1 = \lambda_2 > \lambda_3$) with exponential correlation functions, Gelhar and Axness (1983) obtained:

$$g_{11} = g_{22} = \frac{1}{2}\frac{1}{\rho^2-1}\left[\frac{\rho^2}{\sqrt{\rho^2-1}}\tan^{-1}\left(\sqrt{\rho^2-1}\right) - 1\right]$$

$$g_{33} = \frac{\rho^2}{\rho^2-1}\left[1 - \frac{1}{\sqrt{\rho^2-1}}\tan^{-1}\left(\sqrt{\rho^2-1}\right)\right]$$

where $\rho = \lambda_1/\lambda_3 > 1$. In this study, λ_x and λ_y are averaged to obtain λ_1, representing a horizontal integral scale from modeling an omnidirectional horizontal variogram. For nonsymmetrical structures, g_{jj} can be evaluated by numerical integration. These results have been tested and expanded by prior authors (e.g., Zhang, 2002), and for statistically anisotropic media, have generally been found accurate for low $\ln K$ variances (e.g., less than 1.0). A high-variance version of the above equation also exists based on the Landau–Lifshitz conjecture, which treats the two terms within the brackets of Eq. (15) as part of a series expansion of an exponential function:

$$K_{jj} = K_G \exp\left[\sigma_f^2\left(\frac{1}{2} - g_{jj}\right)\right] \quad (j = 1,\ldots,3) \tag{16}$$

Along the same line of arguments, Ababou (1995) proposed a simplified formula of the above equation:

$$K_{jj} = K_G \exp\left[\sigma_f^2\left(\frac{1}{2} - \frac{1}{3}\frac{\lambda_{Harmo}}{\lambda_j}\right)\right] \quad (j = 1,\ldots,3) \tag{17}$$

Finally, a similar expression to Eq. (16) was also proposed for anisotropic transmissivity fields with arbitrary covariance types (Pozdniakov and Tsang, 1999). In the new formulation, g_{jj} was replaced by g_{scale}, a function that depends on two unknown constants and a multidimensional integral of the $\ln K$ autocorrelation function (see Eq. (21b) in Pozdniakov and Tsang (1999)). The unknown constants were estimatible under limiting conditions (e.g., planar flow, or, $L_z/\lambda_z \to \infty$).

Note that the above equations based on stochastic theories aim to predict an ensemble effective conductivity of a RSF, thus rigorous comparison between upscaled equivalent conductivity with ensemble effective conductivity will require a stochastic Monte Carlo analysis (e.g., Zhang, 2002; Dagan et al., 2004; Frippiat et al., 2009). This may be accomplished by creating a large number of conductivity realizations, e.g., adding a small random component to each synthetic aquifer model. For each realization, an equivalent conductivity can be computed via upscaling. The ensemble conductivity is then obtained by averaging results across all realizations. This, however, would require numerous flow experiments, beyond the scope of the current study. In this study, rather than validating theories, we're interested in whether theories can be used to predict properties consistent with numerical simulation results on single realizations containing geologically complex or "realistic" heterogeneity, following examples of prior studies (e.g., Desbarats and Srivastava, 1991; Zhang et al., 2006, 2007; Zhang and Gable, 2008). Further, within the stochastic framework, an argument can be made that in evaluating single realizations, if the domain size is large compared to $\ln K$ correlation scale, ergodic limit may be reached whereby deterministic spatial average coincides with ensemble average.

2.6. Flow connectivity

For the two select aquifer models, visual inspection suggests differences in connectivity pattern of the conductivity field (Fig. 2), despite their similar univariate and bivariate statistics, i.e., $\ln K$ histograms of both models are approximately Gaussian and $\ln K$ variograms are exponential-like (Figs. 4 and 5). To quantify connectivity (and particular its impact on fluid flow), we followed prior works and identified three fluid flow connectivity factors (CF1, CF2, and CF3) (Knudby and Carrera, 2005, 2006). In general, the higher the flow CF, the higher the degree of conductivity connectivity and associated effects of flow channeling, thus increasing deviation from a multiGaussian field which exhibits maximum spatial disorder rather than connectivity.

CF1 is the directional power-averaging exponent of Eq. (10), i.e., $\omega_j (j = 1,\ldots,3)$:

$$\begin{aligned} \mathrm{CF1}x &= \omega_1 \\ \mathrm{CF1}y &= \omega_2 \\ \mathrm{CF1}z &= \omega_3 \end{aligned} \tag{18}$$

In the subsequent analysis, we will use CF1x to represent ω_1, CF1y to represent ω_2, and CF1z to represent ω_3.

CF2 is the ratio of equivalent conductivity principal component to K_G:

$$\begin{aligned} \mathrm{CF2}x &= K_{11}/K_G \\ \mathrm{CF2}y &= K_{22}/K_G \\ \mathrm{CF2}z &= K_{33}/K_G \end{aligned} \tag{19}$$

where K_{11}, K_{22}, and K_{33} are the principal components of the equivalent conductivity computed with Eq. (2). Note that CF1 and CF2 are related by Eq. (13).

CF3 is the ratio of directional critical path conductivity (K_c) to K_G:

$$\begin{aligned} \mathrm{CF3}x &= K_{cx}/K_G \\ \mathrm{CF3}y &= K_{cy}/K_G \\ \mathrm{CF3}z &= K_{cz}/K_G \end{aligned} \tag{20}$$

where K_{cx}, K_{cy}, and K_{cz} are the directional critical path conductivities along the x, y, and z axis, respectively. The critical path conductivity is the conductivity at the percolation threshold for an indicator transformed field. To determine K_c along a given direction, an indicator transform value of K was adjusted until a minimum was reached at which a high-K path of connected cells first spanned the field along the given direction. GEO_OBJ was used for this identification (Deutsch, 1999). For 3D connectivity, we considered two cells connected only if they share a face, e.g., cells were not considered connected if they only share an edge or a corner point.

Among the three factors, CF1 and CF2 were determined from numerical upscaling for which flow simulations were conducted. CF3 was independent of flow simulations. It describes the *geometric* connectivity among the high-K cells. For a set of two-dimensional data exhibiting connectivity, Knudby and Carrera (2005) evaluated all three factors and found CF2 both sensitive to fluid flow connectivity and the easiest to evaluate. The above authors also observed that CF2 and CF3 exhibited equivalent behaviors. In this study, we evaluated all three CF since the models analyzed are three-dimensional. Connectivity of spatial structures and fluid flow channeling are expected to be sensitive to the third dimension. Each of our flow CF is further directional, corresponding to the principal components of the upscaled conductivity (previous studies had focused on the lateral direction only). Since an earlier two-dimensional analysis had suggested that increasing conductivity variance contributed to increasing effects of flow channeling (Zhang et al., 2007), in this study, all three flow CF will be evaluated at increasing global $\ln K$ variance. At a fixed variance, both the flow CF and the directional percolation clusters (which formed at the critical path conductivities) will be compared between the aquifer models to confirm the observed differences in connectivity.

3. Results and discussion

3.1. Flow simulations

As part of the upscaling procedure, for each model, after the conductivity field was scaled to an appropriate global $\ln K$ variance, three single-phase and steady-state flow simulations were conducted. The simulation results were used to estimate three sets of spatially averaged fluxes and head gradients for Eq. (2), and an upscaled equivalent conductivity was calculated. Before we present the upscaling results, it is of interest to understand the impact of increasing variance on the fluid flow behaviors in each model. Thus, for Model 1, along each of the flow directions (which correspond to specified boundary conditions used in upscaling), both hydraulic head and Darcy flux are visualized (Fig. 6).

In each column of Fig. 6, the same global boundary condition was used: x-flow: first column; y-flow: second column; z-flow: third column. To facilitate comparison between the low variance and high variance systems, in each column, the same legends in head and flux were used. Simulation results pertaining to two variances are shown: $\sigma_f^2 = 0.1$ (top row), and $\sigma_f^2 = 7.0$ (bottom row). Comparing these two, the high-variance field exhibits significant preferential flowpaths for all flow directions simulated. Results pertaining to $\sigma_f^2 = 1.0$ and $\sigma_f^2 = 16.0$ are not shown. The flow behavior of $\sigma_f^2 = 1.0$ lies between those of $\sigma_f^2 = 0.1$ and $\sigma_f^2 = 7.0$ simulations. The flow behavior of $\sigma_f^2 = 16.0$ is more extreme: alongside those of the lower variance systems, its Darcy flux cannot be visualized well using the same legend. However, for all flow directions, it preserves and highlights the same preferential flow behavior as seen in the field with $\sigma_f^2 = 7.0$ (bottom row). The same simulation results are presented for Model 2 (Fig. 7), where preferential flow behavior also exists for the high-variance system, along all flow directions.

Results of both models thus suggest that for a fixed global boundary condition, when $\ln K$ variance becomes high, the flow field becomes increasingly non-uniform. For all flow directions investigated, significant flow channeling occurs, accompanied by an increased spread in the velocity magnitude. Thus, for a fixed heterogeneity pattern, flow connectivity (i.e., effects of fluid channeling) is positively correlated with variance. Later results for each model will indeed confirm that increasing variance results in increasing magnitude of several flow connectivity factors. On the other hand, at the same variability level ($\sigma_f^2 = 7.0$ in Figs. 6 and 7), the characteristics of flow channeling are different between the models. In particular, a flowpath exists along the x axis in Model 1, which is absent in Model 2, while both containing flowpaths in the vertical direction. As part of the CF3 calculations, a percolation cluster analysis confirms the existence of spanning high-K clusters (i.e., geometric connectivity) that correspond to these particular flow pathways. The spanning clusters for Model 1 is shown in Fig. 8. From this figure, significant lateral (along x) and vertical connectivity exist, corresponding to the location of the simulated preferential flowpaths. Thus, at a fixed variance, flow connectivity is also correlated with the existence of geometric connectivity. In Fig. 8, an additional observation is that the spanning cluster along any direction is non-uniformly distributed in space,

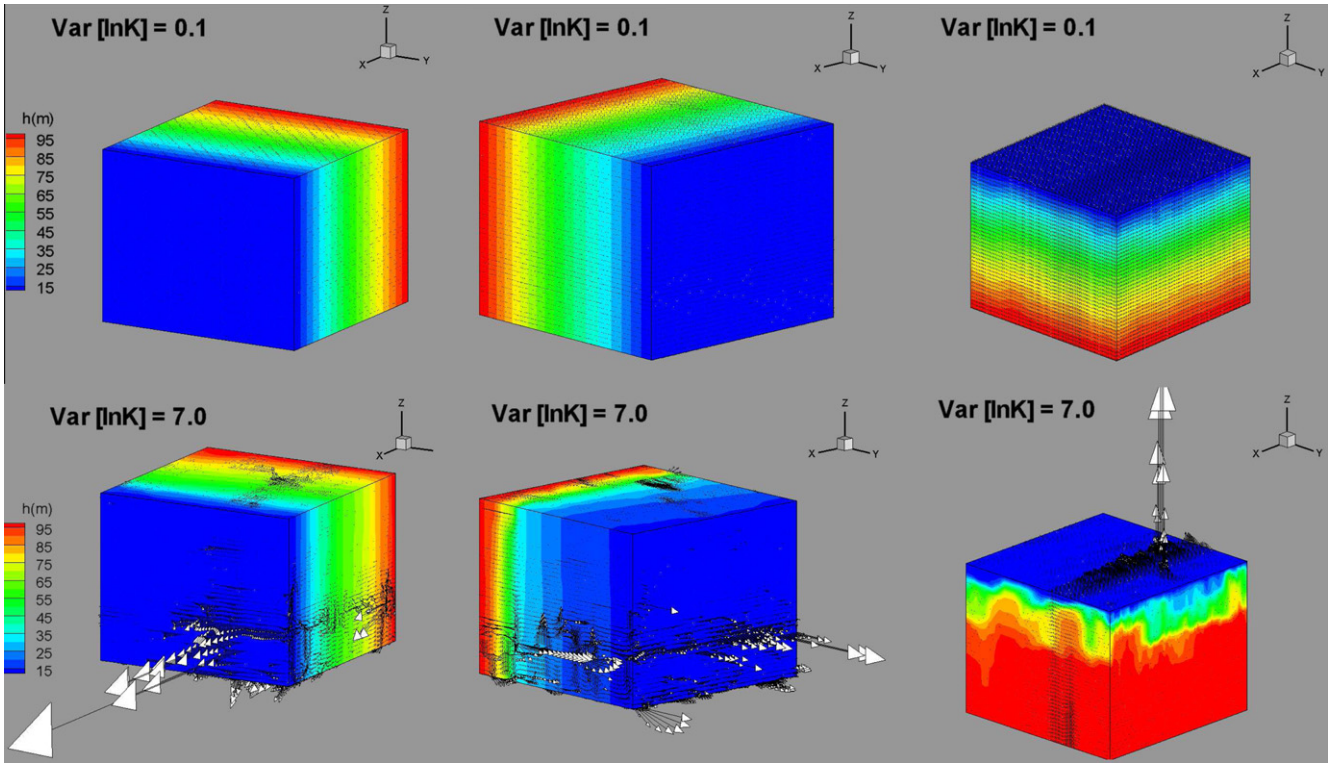

Fig. 6. Simulation results of hydraulic head (contours) and Darcy flux (vectors) for Model 1. The top row has σ_f^2 of 0.1; the bottom row has σ_f^2 of 7.0. The columns are (left to right): *x*-flow, *y*-flow, *z*-flow. In each column, the same legends in head and flux are used.

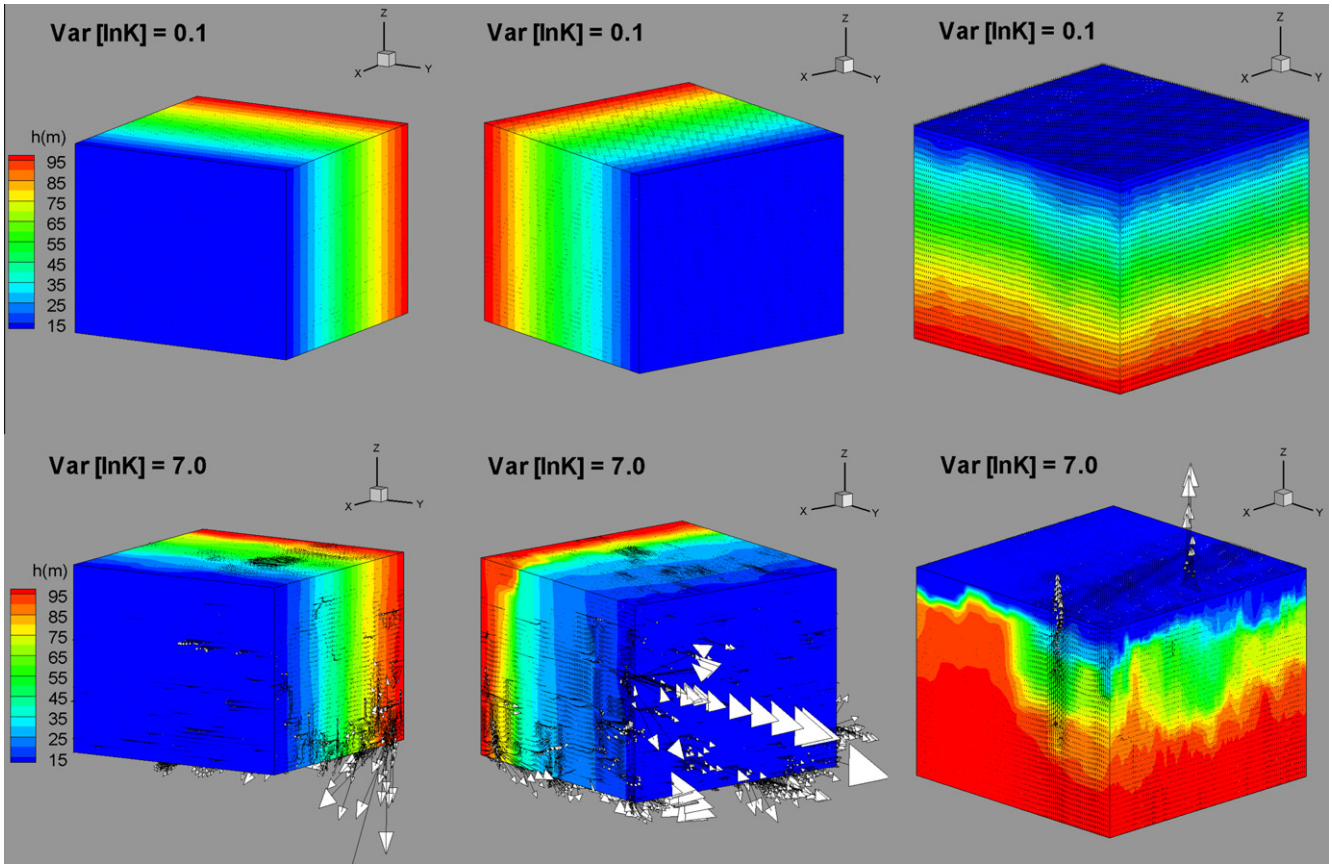

Fig. 7. Simulation results of hydraulic head (contours) and Darcy flux (vectors) for Model 2. The top row has σ_f^2 of 0.1; the bottom row has σ_f^2 of 7.0. The columns are (left to right): *x*-flow, *y*-flow, *z*-flow. In each column, the same legends in head and flux are used.

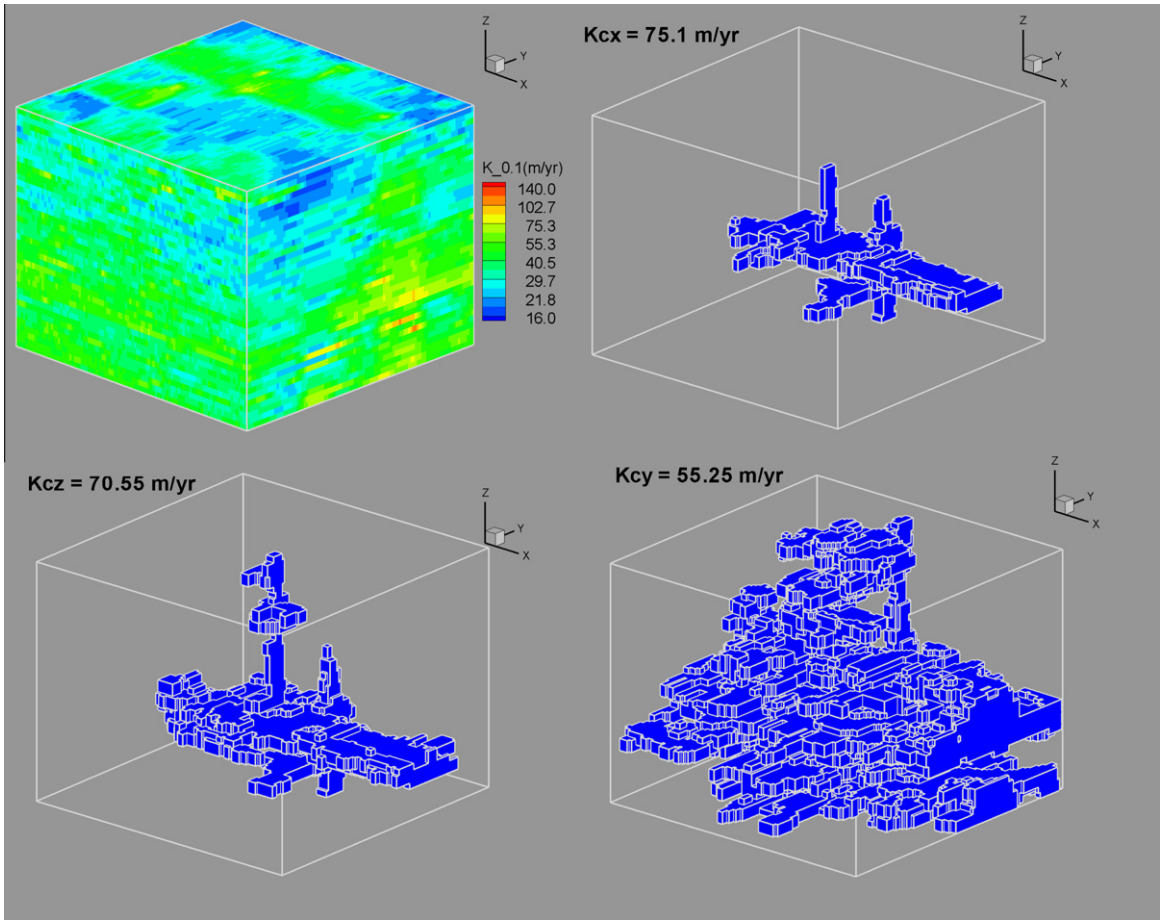

Fig. 8. Geometric connectivity in Model 1 at three directional percolation thresholds, when the global aquifer variance is 0.1. K_{cx}, K_{cy}, and K_{cz} are the directional critical path conductivities along the x, y, and z axes, respectively. Note that the same directional percolation clusters will form at increasing $\ln K$ variances, except the pertinent directional critical path conductivity will increase, its value scaled by the variance based on those of $\sigma_f^2 = 0.1$. This is because topology is not affected by variance scaling.

Table 1
Equivalent hydraulic conductivity (m/yr) computed with Eq. (2) for Model 1 (top panel), its principal components, and the equivalent conductivity computed with the Simple Laplacian method. Also listed is the results of directly averaging the local conductivities: $[K_H, K_G, K_A]$. Results pertaining to Model 2 are shown in the lower panel.

	$\sigma_f^2 = 0.1$			$\sigma_f^2 = 1.0$			$\sigma_f^2 = 7.0$			$\sigma_f^2 = 16.0$		
Model 1												
$\mathbf{K}^*$ [Eq. (2)]	40.968	0.019	−0.003	60.735	0.099	−0.037	514.114	−4.348	−0.284	5200.20	−59.500	−1.800
	0.019	40.101	0.001	0.099	50.321	0.024	−4.348	185.380	1.868	−59.500	706.300	25.000
	−0.003	0.001	38.153	−0.037	0.024	33.434	−0.284	1.868	34.075	−1.800	25.000	89.800
$\mathbf{K}^*$ [principal components]	40.968	0	0	60.736	0	0	514.172	0	0	5201.00	0	0
	0	40.101	0	0	50.320	0	0	185.345	0	0	706.500	0
	0	0	38.153	0	0	33.434	0	0	34.052	0	0	88.800
$\mathbf{K}^*$ [Simple Laplacian]	40.981	0	0	60.747	0	0	512.724	0	0	5183.03	0	0
	0	40.147	0	0	50.432	0	0	185.896	0	0	713.983	0
	0	0.000	38.434	0	0	34.295	0	0	36.176	0	0	96.440
Averages $[K_H, K_G, K_A]$	[37.260, 39.160, 41.160]			[24.280, 39.160, 63.370]			[2.510, 39.160, 803.620]			[0.196, 39.160, 23545.0]		
Model 2												
$\mathbf{K}^*$ [Eq. (2)]	26.529	0.0017	0.0003	39.406	0.041	0.014	299.960	4.000	0.749	2025.70	14.200	6.100
	0.0017	26.262	0.003	0.041	36.455	0.036	4.000	201.871	1.163	14.200	929.800	3.600
	0.0003	0.003	24.526	0.014	0.036	19.804	0.749	1.163	10.229	6.100	3.600	7.800
$\mathbf{K}^*$ [principal components]	26.529	0	0	39.406	0	0	300.125	0	0	2025.90	0	0
	0	26.262	0	0	36.454	0	0	201.715	0	0	929.700	
	0	0	24.526	0	0	19.804	0	0	10.220	0	0	7.800
$\mathbf{K}^*$ [Simple Laplacian]	26.5217	0	0	39.351	0	0	298.329	0	0	2015.59	0	0
	0	26.244	0	0	36.361	0	0	200.853	0	0	926.130	
	0	0	24.558	0	0	19.831	0	0	10.154	0	0	7.719
Averages $[K_H, K_G, K_A]$	[24.139, 25.366, 26.681]			[15.527, 25.366, 42.625]			[0.807, 25.366, 1037.30]			[0.013, 25.366, 89288.00]		

an indicator of non-stationary conductivity. A stationary field, on the other hand, leads to a uniform distribution of the spanning cluster. To summarize, both heterogeneity variance and geometric connectivity contribute to the effects of preferential flow channeling which can occur under different boundary conditions, i.e., global flow field parallel or perpendicular to the angle of stratification.

3.2. Upscaled conductivities

For each model, at increasing variance, the upscaled equivalent conductivities ($\mathbf{K}^*$) computed with Eq. (2) is listed in Table 1. They are full tensors for which the table also lists their principal components. Results of a diagonal tensor computed by the Simple Laplacian method (Wen and Gómez-Hernández, 1996) are presented along with direct averages of local conductivities. For both models and for all variances evaluated, the equivalent conductivities are consistent with those of the Simple Laplacian method (i.e., comparing the principal components of $\mathbf{K}^*$ with the diagonal tensor computed by the later method). For both models, most equivalent conductivities are diagonally dominant, reflecting the near horizontal stratigraphic dip. As variance increases, the off-diagonal components become slightly more important, suggesting that the equivalent conductivity principal axis has experienced minor rotation when variance is very high (i.e., $\sigma_f^2 = 16$). This is likely due to the enhanced local flow channeling effects, i.e., components of cross flow that are not aligned with the global axis become important at high variances. However, when deposits exhibit lateral stratification and $\ln K$ variance is moderate (e.g., less than 7.0), the traditional simulation approach (using diagonal tensors for the grid cells) which assumes global simulation axes aligned with the sub-grid-scale conductivity principal directions should suffice.

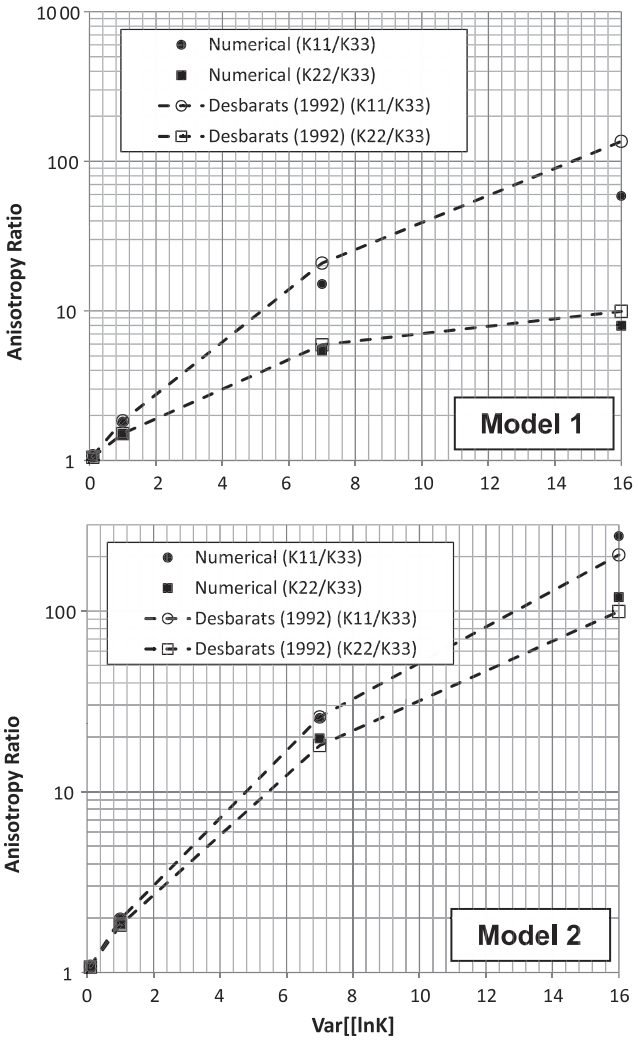

Fig. 9. Equivalent conductivity anisotropy ratios (K_{11}/K_{33}, K_{22}/K_{33}) against theory predictions (Desbarats, 1992) under increasing $\ln K$ variance.

The shape of the tensor (i.e., the relative size of K_{11}, K_{22}, K_{33}, thus the global conductivity anisotropy ratios) is also changing with variance (Fig. 9). For Model 1, K_{11}/K_{33} and K_{22}/K_{33} are, respectively: 1.07 and 1.05 $\left(\sigma_f^2 = 0.1\right)$, 1.81 and 1.51 $\left(\sigma_f^2 = 1.0\right)$, 15.10 and 5.44 $\left(\sigma_f^2 = 7.0\right)$, 58.57 and 7.96 $\left(\sigma_f^2 = 16.0\right)$. For Model 2, K_{11}/K_{33} and K_{22}/K_{33} are, respectively: 1.08 and 1.07, 1.99 and 1.84, 29.37 and 19.74, 259.73 and 119.19. Clearly, for both models, higher variance results in higher anisotropy ratio of the global conductivities. As variance increases, fluid flow becomes increasingly channeled into the high-K connected facies, resulting in increasingly significant lateral flow, while torturous flowpaths in the vertical direction become subdued. In Model 1, the rise of K_{11}/K_{33} with variance is six times faster than K_{22}/K_{33}, most likely due to the existence of a high-K structure which is spanning the domain along the x axis (Fig. 8). This structure acts to focus flow in the x direction, thus enhancing K_{11} and K_{11}/K_{33}. In Model 2, the rise of K_{11}/K_{33} with variance is roughly two times faster than K_{22}/K_{33}. In the percolation analysis, this model lacks an obvious preferential pathways in either direction, i.e., the percolation clusters in x and y directions are rather planar structures (not shown).

3.3. Comparison with analytical predictions

For each model, at increasing variance, the equivalent conductivity principal components were first compared to the Wiener's Bounds and the Cardwell and Parsons bounds (Fig. 10). While all components fall within the Wiener's Bounds, as expected, the lower Cardwell and Parsons bound is often higher than one of the components. When the variance is low (less than 1.0), both lateral components (K_{11} and K_{22}) are very close to K_A. However, they significantly deviate from K_A as variance increases. This differs from the results of an earlier study analyzing a two-dimensional stratigraphy (Zhang et al., 2007). In that study, the maximum (lateral) principal components of different hydrogeological units fall extremely close to the arithmetic mean, for σ_f^2 ranging from 0.31 to 1.85. This suggests that, for deposit with higher variance $\left(\sigma_f^2 > 1.0\right)$, flow connectivity characteristics between two-dimensional and three-dimensional systems are different. In this study, for both models, the lateral equivalent conductivities (K_{11}, K_{22}) increase with variance, while K_{33} fluctuates or decreases with variance. Overall, however, a heuristic relationship between either bounds and the equivalent conductivity principal components cannot be established.

The principal components are then compared to the analytical predictions (Ababou, 1991, 1995; Desbarats, 1992; Gelhar, 1993; Noetinger and Haas, 1996) (Fig. 11). Since theory by Gelhar (1993) is strictly valid for low variances, its predictions were made for models with $\sigma_f^2 = 0.1$ and 1.0 only. The high-variance version of the theory was also tested against the upscaling results and was found inaccurate and thus not presented. For both aquifer models, we find: (1) when $\sigma_f^2 = 0.1$, all methods are almost equally accurate; (2) when $\sigma_f^2 = 1.0$, all methods other than Gelhar (1993) are accurate; (3) for all variances up to 16.0, the formulations proposed by Desbarats (1992) (Eq. (12)) and Noetinger and Haas (1996) (Eq. (13)) are consistently the most accurate. Note that results based on Eq. (13) were not plotted since they vary from the predictions of Eq. (12) by less than 1%. These two formulations are thus considered identical for the range of conductivity varied; and (4) when $\sigma_f^2 > 1.0$, the formulations proposed by Ababou (1991, 1995) consistently overestimate the lateral components and underestimate the vertical component. Using the most accurate formulation, anisotropy ratios of the equivalent conductivity from numerical upscaling and theory predictions are also compared (Fig. 9). Results are again consistent, though for Model 1 at higher variances, some overestimation of K_{11}/K_{33} was made by theory.

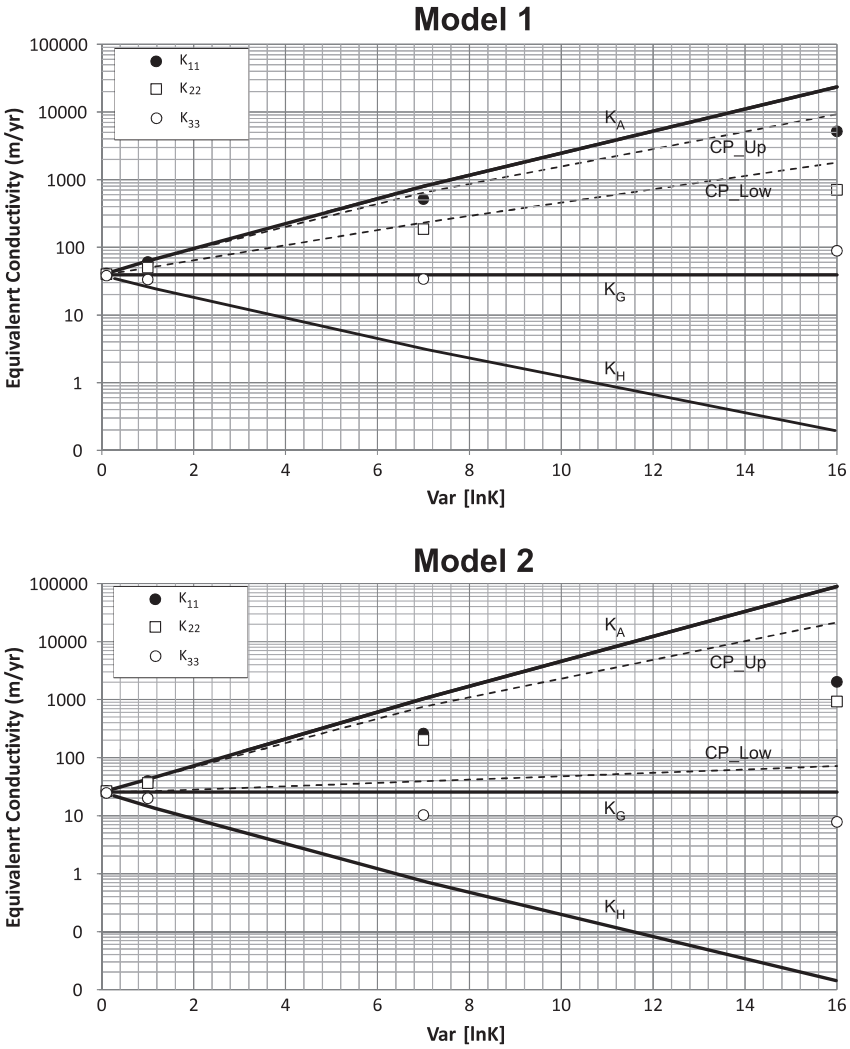

Fig. 10. Equivalent conductivity principal components against the Wiener's Bounds and the Cardwell and Parsons (CP) Bounds under increasing ln*K* variance.

The above finding, besides providing constraints on the range of applicability of different analytical results, is significant since the analytical expressions of Desbarats (1992) and Noetinger and Haas (1996) were developed for multiGaussian media at small variances. Both formulations had been tested numerically and were found accurate for multiGaussian models, at small to moderate variances. Herein, their accuracy is also demonstrated on two non-multiGaussian models exhibiting connectivities and with a range of low-to-high variances. This result, however, is not considered unexpected. Desbarats and Srivastava (1991) had conducted a similar study on a two-dimensional transmissivity field which also exhibited a significant domain-spanning channel. In that study, the authors concluded that "ensemble theoretical models based on perturbation approaches can provide reasonable estimates of general flow and transport properties of single field realizations under moderate conditions of heterogeneity". This statement may sum up our own observations here. Moreover, formulations of Desbarats (1992) and Noetinger and Haas (1996) are based on power-law averaging which proves to be a reliable tool here to predict 3D grid-block equivalent conductivity components, even when sub-grid heterogeneities are non-multiGaussian and of high variance. However, this good match maybe due to multiple factors, including the single realization approach in evaluating ω_j, the fact that global ln*K* histograms of both models are unimodal, and the large domain size compared to ln*K* correlation scales (i.e., the ergodicity assumption). Clearly, grid blocks in large field simulation models may or may not be able to satisfy these requirements. Non-ergodic and multi-modal fields will be investigated in the future. Further, the power-averaging exponents were identified in this study using numerical simulations. Future work will investigate a predictive method for such exponents based on, e.g., a modification of Ababou (1991), although higher-order correlation parameters are likely needed to capture nonlinear connectivity in three-dimensions.

3.4. Flow connectivity

Based on results of conductivity upscaling and percolation analysis, three flow connectivity factors were computed for each model, for increasing ln*K* variance and along each of the coordinate axes (Table 2). For both models, CF1 (power-averaging exponent) ranges from 0.5 to 0.9 in the *x* direction, 0.4 to 0.7 in the *y* direction, and −0.7 to 0.1 in the *z* direction. The conductivity field of each model is statistically anisotropic, thus the power-averaging exponents significantly deviate from 1/3 which is predicted by theory and verified by numerical experiments for 3D statistically isotropic media (Desbarats, 1992).

Results also suggest that only certain connectivity factors increase with variance. For both Model 1 and Model 2, these are: CF2*x*, CF3*x*, CF2*y*, CF3*y*, CF1*z*, and CF3*z*. For the lateral flows

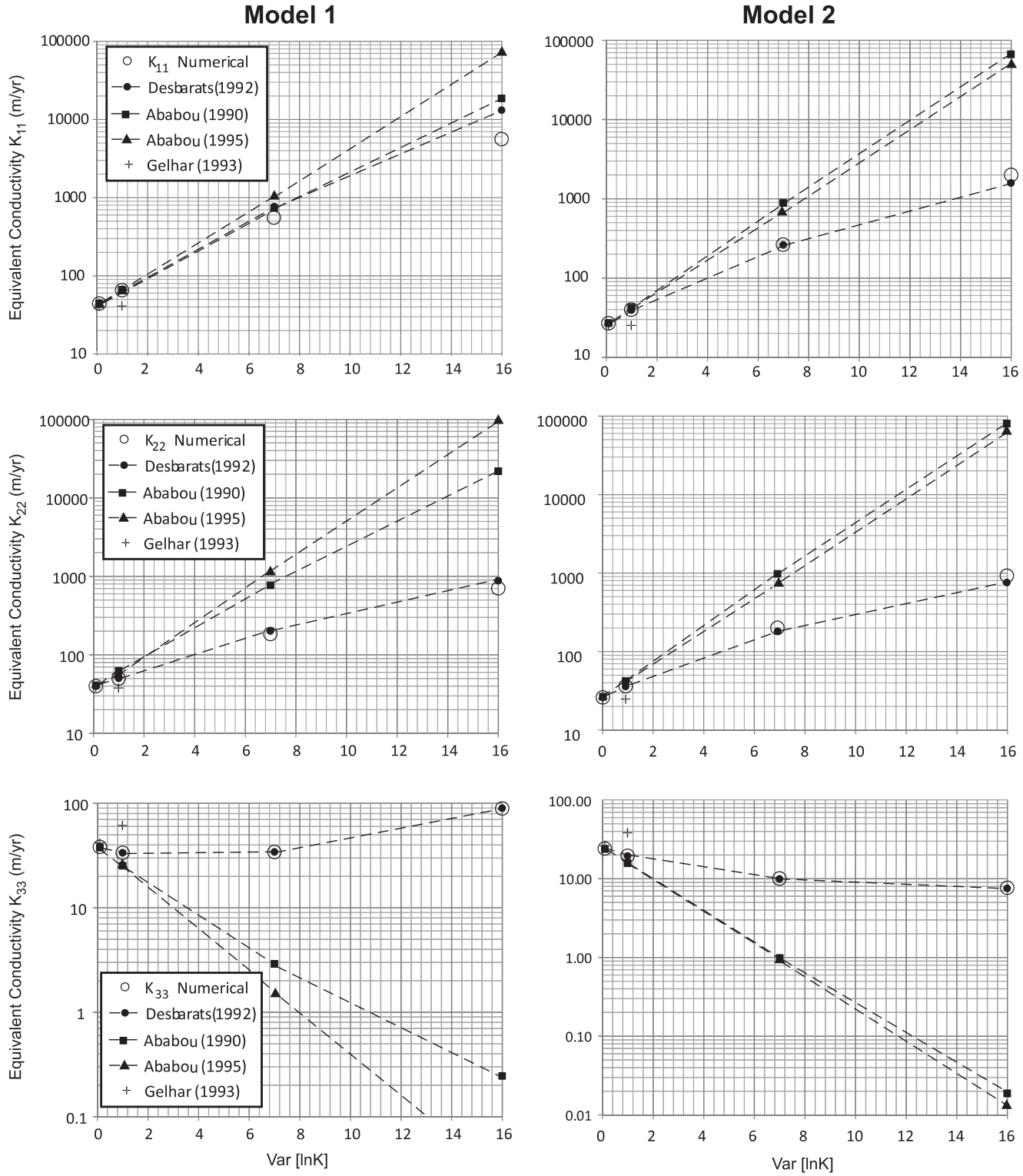

Fig. 11. Equivalent conductivity principal components (empty circles) against theory predictions (solid symbols linked by lines). The first column lists K_{11}, K_{22}, and K_{33} against increasing variance for Model 1. The second column pertains to Model 2.

(i.e., CF2*x*, CF3*x*, CF2*y*, and CF3*y*), this finding is consistent with the results of Knudby and Carrera (2005). Both studies suggest increasing flow channeling in the horizontal direction with increasing variance, which is captured by CF2 and CF3. On the other hand, for both models, CF1*x* decreases with variance while CF1*y* fluctuates with variance. As variance increases, the interval of the local conductivity values to be power-averaged increases. This results in a power exponent that is nonlinear with respect to the equivalent conductivity (note that both K_{11} and K_{22} increase with variance, see Fig. 10). A similar finding was observed in Knudby and Carrera (2005). Both studies suggest that unlike CF2 and CF3, CF1 may not be a useful indicator of flow channeling in the lateral direction. For example, in statistically isotropic media with infinite horizontal extent, power-averaging exponent was found to depend on the ratio of aquifer thickness and λ_z (Pozdniakov and Tsang, 1999). To understand its behavior in anisotropic media, additional studies

Table 2
Flow connectivity factors (CF) for Model 1 at increasing ln*K* variances (top panel). Results pertaining to Model 2 are shown in the lower panel. For CF that increases with variance, the values are highlighted with italic bold.

Var[ln *K*]	CFl*x*	CF2*x*	CF3*x*	CFl*y*	CF2*y*	CF3*y*	CFl*z*	CF2*z*	CF3*z*
Model 1									
0.1	0.907	***1.046***	***1.918***	0.477	***1.024***	***1.411***	***−0.521***	0.974	***1.802***
1.0	0.906	***1.551***	***7.840***	0.507	***1.285***	***2.970***	***−0.317***	0.854	***6.434***
7.0	0.828	***13.130***	***232.397***	0.469	***4.733***	***17.820***	***−0.040***	0.870	***137.723***
16.0	0.717	***132.814***	***3778.341***	0.390	***18.041***	***77.838***	***0.103***	2.268	***1714.282***
Model 2									
0.1	0.889	***1.046***	***1.519***	0.689	***1.035***	***1.519***	***−0.678***	0.967	***1.364***
1.0	0.853	***1.554***	***3.752***	0.707	***1.437***	***3.752***	***−0.501***	0.781	***2.670***
7.0	0.666	***11.833***	***33.071***	0.562	***7.953***	***33.071***	***−0.264***	0.403	***13.447***
16.0	0.515	***79.880***	***198.236***	0.425	***36.657***	***198.236***	***−0.150***	0.308	***50.853***

will be needed by varying the domain length scales against ln*K* integral scales.

For the vertical flow, however, with increasing variance, CF1*z* of both models indicates that the equivalent vertical conductivity approaches K_G from K_H (note that under mean uniform flow conditions, K_G is equivalent conductivity of a 2D horizontal aquifer of uniform thickness with statistically isotropic correlation, K_H is equivalent conductivity for flow perpendicular to perfect stratification). This implies increasing disorder in flow continuity along the vertical direction with increasing variance. A similar trend exists for CF2*z* in Model 2, but not for Model 1, while an opposite trend is observed for CF3*z*. Clearly, the interpretation of vertical flow continuity with variance is not as straightforward as it is for lateral flows (i.e., flow parallel to stratification). The relation between vertical flow factors with variance appears process-dependent, and it is likely affected by the specific heterogeneity pattern investigated.

To examine potential correlation among the lateral flow connectivity factors, CF2 and CF3 are cross-plotted (Fig. 12). Results suggest that: (1) CF3 of each model increases with CF2, consistent with the findings of Knudby and Carrera (2005). Both studies suggest that CF2 and CF3 may be interchangeable in terms of describing lateral flow channeling effects: higher value of either factor corresponds to more significant channeling. Since CF2 is based on flow simulation and upscaling while CF3 based on topological analysis, a useful avenue for future research is to predict the former (thus equivalent conductivity) based on topological parameters, as was done by Samouelian et al. (2007), (2) for Model 1, CF3 along

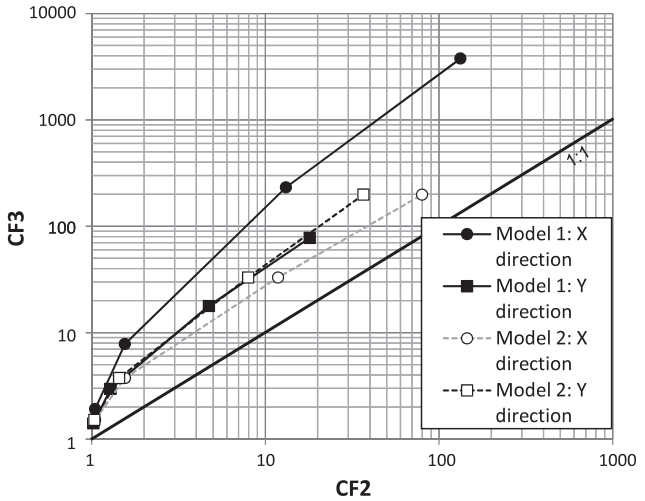

Fig. 12. CF2 versus CF3 cross plot for lateral flows (i.e., *x* and *y* directions). Results for both Model 1 and Model 2 are shown. CF2 is the equivalent conductivity normalized by K_G, CF3 is the critical path conductivity normalized by the same K_G. CF3 is found to be always higher than CF2, above the 1:1 line.

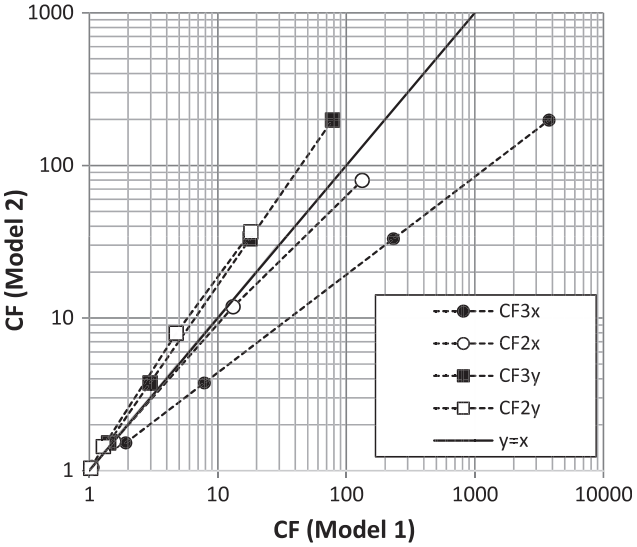

Fig. 13. CF for the lateral flows (i.e., *x* and *y* directions) for Model 1 versus Model 2.

the *x* direction (filled circles) is higher than CF3 along the *y* direction (filled boxes). This can be explained by the existence of a spanning cluster along the *x*-axis (at the same K_{cx}, this cluster is absent in the *y* direction). For Model 2, this difference is smaller, as the lateral connectivity in terms of directional percolation is similar in both directions, and (3) since both CF2 and CF3 are dimensionless, they can be used to compare between heterogeneities. CF3*x* of Model 1 (filled circles) is always greater than CF3*x* of Model 2 (empty circles), while CF3*y* of Model 1 (filled boxes) is nearly identical with CF3*y* of Model 2 (empty boxes). The former can again be explained by the *x*-direction spanning cluster in Model 1. Both models do not contain significant connectivity in the *y* direction, thus the same CF3*y*. This interpretation is confirmed by cross-plotting the lateral CF between Model 1 and Model 2 (Fig. 13). This figure suggests that both CF2 and CF3 can be used to distinguish the larger connectivity along the *x* direction in Model 1 (filled and empty circles, all falling beneath the $y = x$ line). The similar trajectory for the *y*-direction CF (filled and empty boxes) indicates similar connectivity pattern in the *y* direction in the two models. To summarize, directional differences in lateral flow connectivity can be identified by either CF2 or CF3 by comparing the values computed for each model along each of the principal directions.

4. Summary and conclusions

In this study, based on a three-dimensional experimental stratigraphy, two synthetic aquifer models were evaluated for

both upscaled conductivity and fluid flow connectivity. Both aquifer models exhibit statistical anisotropy which is characteristic of fluvial sedimentary systems. Model 1 in particular contains a high-K structure with significant lateral connectivity which cannot be captured by univariate and bivariate statistics. A 3D numerical upscaling method was used to compute a full-tensor equivalent conductivity for each model. Increasing $\ln K$ variances were evaluated: $\sigma_f^2 = 0.1, 1.0, 7.0, 16.0$, reflecting the variability ranges of natural deposits. The numerical upscaling results were verified by comparing against those of an established method which gives the diagonal tensor components. The equivalent conductivities were compared to direct averages of local conductivities, and, to an effective conductivity predicted by several analytical methods. For each model, three fluid flow connectivity factors (CF) were further defined and computed. The impact of variance on both upscaled conductivity and fluid flow connectivity was evaluated.

Based on the above analysis, several conclusions were reached: (1) the 3D upscaling method yielded reliable results of full-tensor equivalent conductivity, (2) for both aquifer models, when the $\ln K$ variances are low (less than 1.0), all analytical methods evaluated are nearly equally accurate; however, when variance is higher, the analytical methods of Desbarats (1992) and Noetinger and Haas (1996) were found to provide robust estimates of equivalent conductivities, despite the possible violation of the multiGaussian assumption, (3) fluid flow characteristics in each model were significantly impacted by increasing variance, which can result in flow channeling in the lateral direction and increasing global anisotropy ratios of the equivalent conductivity. Among the lateral flow connectivity factors analyzed, both the equivalent conductivity, normalized by the geometric mean of local conductivities (CF2), and the critical path conductivities, normalized by the same geometric mean (CF3), were found to increase with variance. Thus, a positive correlation exists between these two connectivity factors, and (4) geometric connectivity, as analyzed by a percolation cluster analysis, indicates the importance of such features in focusing flow, thus both high variance and geometric connectivity contribute to preferential flow channeling.

The above insights are applicable to two specific heterogeneity patterns, scaled at increasing variances. Whether the insights can be extended to other patterns (e.g., significant curvilinear features, bimodal or multimodal $\ln K$ histograms, non-ergodic condition) will be determined in future studies. It is important to point out that the numerical upscaling method of this study is applicable to computing equivalent conductivities for irregularly shaped geological deposits. For example, Eq. (2) can be assembled for a group of cells that belong to a particular facies. This was demonstrated for a hierarchical two-dimensional deposit in Zhang et al. (2006), where $\mathbf{K}^*$ was upscaled for various facies- and formation-scale hydrogeological units. Future work will upscale the sub-aquifer zones in the 3D models, based on either geological interpretations (e.g., different facies: channel, floodplain, sheetflow), percolation characteristics (e.g., spanning clusters at the critical path conductivities), or simulator requirements (e.g., creating layer-cake model layers irrespective of facies or cluster definitions). The impact of different upscaling strategies on the accuracies of both the equivalent conductivities and the homogenized models using them will help answer: what is an optimal method and associated level of heterogeneity homogenization to simulate fluid flow in 3D heterogeneous systems? A related question will address the problem of upscaling for solute transport at multiple scales, following Zhang et al. (2007). In that study, macrodispersivity was analyzed for distinct facies units for a two-dimensional dataset. The extension of the method to three-dimensions to evaluate conductivity models with or without significant geometric connectivity will be of interest.

Acknowledgements

We are grateful to Jim Mullin and Chris Ellis for the indispensable technical assistance with the sediment transport experiment. Funding for the experiment was provided by NSF Grants EAR-9725989 and OCE-0082483, through the Office of Naval Research under Grant N00014-99-1-0603, and by the St. Anthony Falls Industrial Consortium (ExxonMobil, ConocoPhillips, JOGMEC and Chevron). Funding for the numerical study was provided in part by a NSF grant EAR-0838250 awarded to Ye Zhang. The manuscript has benefited from the detailed and insightful comments made by Dr. Alexandre Desbarats of the Geological Survey of Canada and two anonymous reviewers.

References

Ababou, R., 1991. Identification of effective conductivity tensor in randomly heterogeneous and stratified aquifers. In: Proceedings of the 5th Canadian/American Conference on Hydrogeology: Parameter Idenfitication and Estimation for Aquifer and Reservoir Characterization, pp. 155–157.

Ababou, R., 1995. Random Porous Media Flow on Large 3-D Grids: Numerics, Performance and Application to Homogenization (Chapters: Environmental Studies: Mathematical, Computational and Statistical Analysis). Springer-Verlag, New York. pp. 1–25.

Cazanacli, D., Paola, C., Parker, G., 2002. Experimental steep, braided flow: application to flooding risk on fans. Journal of Hydraulic Engineering 128, 322–330.

Chen, Y., Durlofsky, L., 2006. Adaptive local–global upscaling for general flow scenarios in heterogeneous formations. Transport in Porous Media 62, 157–185.

Christie, M.A., 1996. Upscaling for reservoir simulations. Journal of Petroleum Technology 48, 1004–1010.

Christie, M.A., Blunt, M.J., 2001. Tenth spe comparative solution project: a comparison of upscaling techniques. SPE Reservoir Evaluation and Engineering 4, 308–317.

Coskun, S., Wardlaw, N., 1992. Estimation of permeability from image analysis of reservoir sandstones. Journal of Petroleum Science and Engineering 10, 1–16.

Dagan, G., 1989. Flow and Transport in Porous Formations. Springer-Verlag.

Dagan, G., Fiori, A., Jankovic, I., 2004. Transmissivity and head covariance for flow in highly heterogeneous aquifers. Journal of Hydrology 294, 39–56.

Desbarats, A., 1992. Spatial averaging of hydraulic conductivity in three-dimensional heterogeneous porous media. Mathematical Geology 24, 249–267.

Desbarats, A., Srivastava, R., 1991. Geostatistical analysis of groundwater flow parameters in a simulated aquifer. Water Resources Research 27, 687–698.

Deutsch, C.V., 1999. Fortran programs for calculating connectivity of three-dimensional numerical models and for ranking multiple realizations. Computer and Geosciences 24, 69–76.

Deutsch, C.V., 2002. Geostatistical Reservoir Modeling. Oxford University Press.

Deutsch, C.V., Journel, A.G., 1997. GSLIB: Geostatistical Software Library and User's Guide. Oxford University Press.

Durlofsky, L.J., 1991. Numerical calculation of equivalent grid block permeability tensors for heterogeneous porous media. Water Resources Research 27, 699–708.

Durlofsky, L.J., 2005. Upscaling and gridding of fine scale geological models for flow simulation. In: Proceedings, 8th International Forum on Reservoir Simulation, Stresa, Italy, June 20–25.

Frippiat, C., Illangasekare, T., Zyvoloski, G., 2009. Anisotropic effective medium solutions of head and velocity variance to quantify flow connectivity. Advance in Water Resources 32, 239–249.

Gelhar, L., 1993. Stochastic Subsurface Hydrology. Prentice Hall.

Gelhar, L., Axness, C., 1983. Three-dimensional stochastic analysis of macrodispersion in aquifers. Water Resources Research 19, 161–180.

Gerritsen, M.G., Durlofsky, L.J., 2005. Modeling fluid flow in oil reservoirs. Annual Review of Fluid Mechanics 37, 211–238.

Gomez-Hernandez, J., Wen, X., 1998. To be or not to be multiGaussian? – a reflection on stochastic hydrogeology. Advance in Water Resources 21, 147–161.

Hickson, T.A., Sheets, B.A., Paola, C., Kelberer, J.M., 2005. Experimental test of tectonic controls on three-dimensional alluvial facies architecture. Journal of Sedimentary Research 75, 710–722.

Hurst, A., Rosvoll, K., 1991. Permeability Variations in Sandstones and their Relationship to Sedimentary Structures (Chapter: Reservoir Characterisation II). Academic Press.

Kerrou, J., Renard, P., Hendricks Franssen, H., Lunati, I., 2008. Issues in characterizing heterogeneity and connectivity in non-multiGaussian media. Advance in Water Resources 31, 147–159.

Knudby, C., Carrera, J., 2005. On the relationship between indicators of geostatistical, flow and transport connectivity. Advances in Water Resources 28, 405–421.

Knudby, C., Carrera, J., 2006. On the use of apparent hydrauilc diffusivity as an indicator of connectivity. Journal of Hydrology 329, 377–389.

Makse, H., Davis, G.W., Havlin, S., Ivanov, P., King, P., Stanley, H., 1996. Long-range correlation in permeability fluctuations in porous rock. Physical Review E 54, 3129–3134.
Moreton, D., Ashworth, P., Best, J., 2002. The physical scale modeling of braided alluvial architecture and estimation of subsurface permeability. Basin Research 14, 265–285.
Noetinger, B., Haas, A., 1996. Permeability Averaging for Well Tests in 3d Stochastic Reservoir Models, SPE, Paper Number 36653, pp. 919–925.
Paleologos, E.K., Neuman, S.P., Tartakovsky, D., 1996. Effective hydraulic conductivity of bounded, strongly heterogeneous porous media. Water Resources Research 32, 1333–1341.
Paola, C., 2000. Quantitative models of sedimentary basin filling. Sedimentology 47, 121–178.
Pickup, G., Hern, C., 2002. The development of appropriate upscaling procedures. Transport in Porous Media 46, 119–138.
Pickup, G., Ringrose, P., Jensen, J., Sorbie, K., 1994. Permeability tensors for sedimentary structures. Mathematical Geology 26, 227–250.
Pozdniakov, S., Tsang, C.-F., 1999. A semi-analytical approach to spatial averaging of hydraulic conductivity in heterogeneous aquifers. Journal of Hydrology 216, 78–98.
Renard, P., de Marsily, G., 1997. Calculating equivalent permeability: a review. Advances in Water Resources 20, 253–278.
Rubin, Y., Dagan, G., 1988. Stochastic analysis of boundary effects on head spatial variability in heterogeneous aquifers: 1 constant head boundary. Water Resources Research 24, 1689–1697.
Samouelian, A., Vogel, H.-J., Ippisch, O., 2007. Upscaling hydraulic conductivity based on the topology of the sub-scale structure. Advances in Water Resources 30, 1179–1189.
Sanchez-Vila, X., Guadagnini, A., Carrera, J., 2006. Representative hydraulic conductivities in saturated groundwater flow. Reviews of Geophysics 44. 2005RG000, 169.
Sarris, T.S., Paleologos, E.K., 2004. Numerical investigation of the anisotropic hydraulic conductivity behavior in heterogeneous porous media. Stochastic Environmental Research 18, 188–197.
Scheibe, D.T., Freyberg, D.L., 1995. Use of sedimentological information for geometric simulation of natural porous media structure. Water Resources Research 31, 3259–3270.
Sheets, B.A., Hickson, T., Paola, C., 2002. Assembling the stratigraphic record: depositional patterns and time-scales in an experimental alluvial basin. Basin Research 14, 287–301.
Sheets, B.A., Paola, C., Kelberer, J.M., 2007. Creation and preservation of channel-form sand bodies in an experimental alluvial system. International Association of Sedimentologists Special Publication 38, 555–567.
Strong, N., Sheets, B.A., Hickson, T.A., Paola, C., 2005. A mass-balance framework for quantifying downstream changes in fluvial architecture. Fluvial Sedimentology VII, 243–253.
Tidwell, V., Wilson, J., 1997. Laboratory method for investigating permeability upscaling. Water Resources Research 33, 1607–1616.
Wen, X.-H., Gómez-Hernández, J., 1996. Upscaling hydraulic conductivities in heterogeneous media: an overview. Journal of Hydrology 183.
Wen, X., Chen, Y., Durlofsky, L., 2006. Efficient three-dimensional implementation of local–global upscaling for reservoir simulation. SPE Journal 11, 443–453.
Zhang, D., 2002. Stochastic Methods for Flow in Porous Media, Coping with Uncertainties. Academic Press.
Zhang, Y., 2008. Hierarchical geostatistical analysis of an experimental stratigraphy. Mathematical Geoscience. doi:10.1007/s11004-008-9180-6.
Zhang, Y., Gable, C.W., 2008. Two-scale modeling of solute transport in an experimental stratigraphy. Journal of Hydrology 348, 395–411. doi:10.1016/j.jhydrol.2007.10.017.
Zhang, Y., Person, M., Merino, E., Szpakiewcz, M., 2005a. Evaluation of soluble benzene migration in the Uinta Basin. Geofluids 5, 106–123.
Zhang, Y., Person, M., Paola, C., Gable, C., Wen, X.-H., Davis, J., 2005b. Geostatistical analysis of an experimental stratigraphy. Water Resources Research 41, w11416. doi:10.1029/2004WR003756.
Zhang, Y., Gable, C.W., Person, M., 2006. Equivalent hydraulic conductivity of an experimental stratigraphy—implications for basin-scale flow simulations. Water Resources Research 42, w05404. doi:10.1029/2005WR004720.
Zhang, Y., Person, M., Gable, C.W., 2007. Representative hydraulic conductivity of hydrogeologic units: insights from an experimental stratigraphy. Journal of Hydrology 339, 65–78. doi:10.1016/j.jhydrol.2007.03.007.